Supplementary Information (SI) for Inorganic Chemistry Frontiers. This journal is © the Partner Organisations 2025

Supporting Information

Polyoxoniobates with the long-sought feature of face-sharing octahedra stabilized by Te(IV): a synthetic analogue of natural minerals

Ni Zhen,^{†a} Run-Han Li,^{†b} Binghui Xue,^{†c} Jingjing Liu,^b Shan Xu,^b Chao Zhang,^d Peng Lei,^a Jing Dong,^a Yingnan Chi,^{*a} Panchao Yin,^{*c} Ya-Qian Lan,^{*b} and Changwen Hu^c

- ^a Key Laboratory of Cluster Science Ministry of Education, Beijing Key Laboratory of Photoelectronic/Electrophotonic Conversion Materials, School of Chemistry and Chemical Engineering, Beijing Institute of Technology, Beijing, 100081, P. R. China.
- ^b School of Chemistry, South China Normal University, Guangzhou, 510006, P. R. China
- ^c South China Advanced Institute for Soft Matter Science and Technology, South China University of Technology, Guangzhou, 510640, P. R. China.
- ^d Henan Key Laboratory of Polyoxometalate Chemistry, Henan University, Henan, 450046, P. R. China.

TABLE OF CONTENTS

I. Experimental section	S3
II. Synthetic discussion	S5
III. Crystallographic studies	S5
IV. Detailed views of structures	S10
V. Supplementary physical characterizations	S15
VI. Mass spectrometric study of compounds in water	S18
VII. The computing method for volume fractions of different PC	ONb species in
solution	S24
VIII. Computational details, EDA analysis, and frontier molecu	lar orbitals of
different PONb species	S26
IX. Photocatalytic hydrogen evolution performance	S29

I. Experimental section

Materials and Methods. Most of reagents and solvents were commercially purchased and used without further purification. K₇HNb₆O₁₉·13H₂O was prepared following literature methods, and the identity was confirmed by IR spectrum.^[1] Inductively coupled plasma mass spectrometry (ICP-MS) was performed on a Thermo Scientific iCAP Q; C, H, N were determined by an ElementarVario EL cube Elmer CHN elemental analyzer. The IR spectra were recorded on a Bruker FT-IR spectrophotometer using KBr pellets as background in the range of 400-4000 cm⁻¹. TGA were performed in flowing N₂ at a heating rate of 10 °C·min⁻¹ on a LABSYS EVO analyzer instrument. XPS analysis was conducted on a PHI 5000 VersaProbe III spectrometer. Capillary electrophoresis experiments were performed in a capillary electrophoretic apparatus UC 7010 equipped with fused-silica capillaries. ESI-MS was performed on AB SCIEX triple TOF 4600 spectrometer operating in resolution mode. The UV-vis spectroscopy of 1 in aqueous solution was performed on Techcomp UV 2600 spectrophotometer. The amount of H₂ produced was determined by gas chromatography (GC-7920, Aulight Co.,) equipped with a thermal conductivity detector (TCD). SEM-EDS measurements were performed on a JOEL JSM-7500F operated at 5 kV. Samples were sputtercoated with Au prior to analysis to enhance conductivity.

Synthesis of $K_{18}Na_{10}H_{11}[(Nb_{13}O_{42})\{Te_3(B-\alpha-TeNb_9O_{33})\}_4]\cdot 65H_2O$ (1). $K_7HNb_6O_{19}\cdot 13H_2O$ (0.535 g, 0.39 mmol), Na_2TeO_3 (0.129 g, 0.583 mmol), $NaHCO_3$ (0.122 g, 1.45 mmol) and KCl (0.1 g, 1.34 mmol) were mixed in 6 mL $Na_2CO_3/NaHCO_3$ buffer solution (0.05 M, pH = 10.00). After stirring at room temperature for one hour, the pH was adjusted to 10.50 using 1 M NaOH. The resulting mixture was sealed in a 23 mL Teflon-lined autoclave and kept at 160 °C for 5 days. After slowly cooling to room temperature (5 °C min⁻¹), the crystals of sandwich-type PONb, $Na_5K_7H_4[(NbO)_6(\alpha-TeNb_9O_{33})_2]\cdot nH_2O$ (~8 mg), was directly obtained. After filtration, the resulting reaction solution was left for crystal growth under ambient conditions in a 25 mL beaker. After 4-5 days, colorless crystals of 1 with octahedral shape were isolated in ~10.2% yield (based on Te). Anal. Calcd (%) for 1: K, 6.12; Na, 2.00; Nb, 39.61; Te, 17.76; H, 1.24. Found: K, 6.33; Na, 2.20; Nb, 39.39; Te, 17.71; H, 1.37. FT-IR (cm⁻¹): 3406 (s), 1632 (s), 887 (m), 793 (s), 725 (s), 636 (m), 532 (m).

Synthesis of $K_{20}Na_5H_{17}[(Nb_{10}O_{36})\{Te_3(B-α-TeNb_9O_{33})\}_4]\cdot 70H_2O$ (2). Compound 2 was prepared following the procedure similar to that of 1, but TeO₂ (0.093 g, 0.583 mmol) was used instead of Na₂TeO₃. After 7 days of evaporation, rhombus rod-like crystals of 2 were collected (yield: ~9.9% based on Te). Anal. Calcd (%) for 2: K, 7.00; Na, 1.03; Nb, 38.23; Te, 18.26; H, 1.42. Found: K, 6.88; Na, 1.07; Nb, 38.64; Te, 18.56; H, 1.21. FT-IR (cm⁻¹): 3436 (s), 1636 (m), 1395 (m), 1041 (w), 872 (w), 784 (s), 744 (s), 636 (m), 557 (w).

X-ray Crystallography. A Bruker APEX-II DUO CCD single-crystal diffractometer with graphite-monochromated Mo Kα radiation (λ = 0.71073 Å) was used to collect the crystallographic data of the two compounds at 296 K. The single crystals were mounted in a Hampton cryoloop with oil to prevent the loss of lattice water molecules. Their structures were solved by direct methods and refined by full-matrix least-squares techniques using the SHELXL-2018/3 and Olex program. Absorption corrections were applied using multi-scan techniques. The H atoms of the lattice water are not located, and all heavy atoms were refined with anisotropic thermal parameters. The residual disordered or crystal water and cations were estimated from PLATON squeeze. And angles (deg) of 1 and 2 are listed in Table S3. BVS results of Te atoms and protonated O atoms for compounds 1-2 are listed in Table S5. The crystallographic data have been deposited with the Cambridge Crystallographic Data Centre (CCDC) as entries 2221182 (1), 2221070 (2).

Electrospray Ionization Mass Spectrometry. All samples were prepared by dissolving in pure water to a concentration of ca. 1×10^{-5} M and injected directly at a flow rate of 5 μ L min⁻¹ using a

syringe pump. All spectra were collected in negative ion mode. For all measurements the following parameters were employed: capillary voltage: 3.0 kV; sample cone voltage: 10 V; extraction cone voltage: 1 V; source temperature: 25 °C; desolvation temperature: 25 °C; cone gas flow: 15 L h⁻¹ (N₂); desolvation gas flow: 750 L h⁻¹ (N₂).

Preparation of Tetrabutylammonium (TBA) Salt of 1 (TBA-1). 1 (5 mg) was dissolved in 5 mL of Na₂CO₃/NaHCO₃ buffer solution (0.05 M, pH = 10.50). Then tetrabutylammonium bromide (TBABr, 400 mg) was added to this colorless aqueous solution, and white precipitation was formed gradually. The precipitation of **TBA-1** was collected by centrifugation, washed with EtOH and dried in a vacuum drying oven.

Capillary Electrophoresis. The capillary electrophoresis test was performed on bare-fused silica capillary (50 μ m i.d., effective length 40 cm) at 200 nm detection wavelength. The running buffer for CE separation was 20 mM Na₂CO₃/NaHCO₃ buffer (pH 10.53). The separation voltage was set at -20 kV. The sample was injected into the capillary (0.5 psi, 5 s). The concentration of 1 was 1.31 mg/mL and the temperature was 25 °C.

Small Angle X-ray Scattering. The SAXS experiment was performed at the beamline BL19U2 of Shanghai Synchrotron Radiation Facility and the HomeLab of Rigaku. The Samples for SAXS test were injected into PMMA cells covered with 3M tape after filtration through 220 nm membrane. We used Oligomer in the ATSAS package to fit the SAXS curve, and the fitting function is

 $I(q) = \sum_{i} V_i \times I_i(q)$, where V_i and $I_i(q)$ are the volume fraction and the scattering intensity from the i-th component, respectively.

Photocatalytic H₂ evolution experiments. The photocatalytic H₂ production experiments were performed in a sealed 50 mL Pyrex flask. A 300 W Xe lamp with a wavelength range from 300 to 1100 nm was used as the light source to trigger the photocatalytic reaction. The reaction temperature was controlled at 298 K using the cooling water circulation. The visible-light-driven (>300 nm) H₂ evolution activity of 1 were examined using MeCN/H₂O as solvent, [Ru(bpy)₃]Cl₂·6H₂O as a photosensitizer, triethylamine (TEA) as a sacrificial electron donor, and 1 as a water reduction catalyst (WRC). In a typical experiment, photocatalyst (10 mg) and photosensitizer (10 mg) was added into the mixed solution which contained $H_2O/MeCN/TEA$ (30 mL, v/v = 4:1:1). Before irradiation, the system was degassed with argon (Ar) to remove dissolved O₂ for 30 min. To detect the formation of hydrogen from the reaction mixture, 500 µL from the middle of the reactor was taken out with a syringe and injector into a GC with a TCD detector, using Ar as the carrier gas and reference gas. Sampling was performed at an interval of 1 h over 4 h during the reaction. All glassware was carefully rinsed with ultrapure water prior to usage. The photocatalytic stability tests were performed using the same processing parameters. The homogeneous solution immediately after the reaction was mixed with pure acetonitrile solvent (300 mL) and the solids precipitated in this solution were used for further characterization and test in photocatalytic reaction.

Electrochemistry measurements. The photocurrent-time (I-T) profile was recorded on the CHI 660E electrochemical workstation with a standard three-electrode system with the photocatalyst-coated ITO as the working electrode, Pt plate as the counter electrode, and an Ag/AgCl as the reference electrode. A 0.5 M Na₂SO₄ solution was used as the electrolyte.

Preparation of the working electrode: 2 mg photocatalyst were dispersed in a mixed solution of 990 μ L ethanol and 10 μ L Nafion D-520 dispersion solutions to generate a homogeneous slurry. Subsequently, 200 μ L of slurry was transferred and coated on ITO glass plates (1 cm \times 2 cm) then dried at room temperature.

II. Synthetic discussion

The synthesis of compounds 1 and 2 combines hydrothermal treatment and evaporation method. The starting materials of compound 1 are K₇HNb₆O₁₉·13H₂O, Na₂TeO₃, NaHCO₃ and KCl. Compound 2 was prepared using a procedure very similar to that of 1 by replacing Na₂TeO₃ with TeO₂ and extending evaporation time. Occasionally, compound 1 crystallized during the slow evaporation process when TeO₂ was used as tellurium source, but compounds 2 and 1 never crystallized together in one reaction. They can be easily distinguished by their unique crystal morphology and we were able to obtain one compound without co-crystallization with the other. We found that the synthesis of 2 was less reproducible, sensitive to the evaporation conditions, such as temperature and humidity of the lab. The self-assembly process for POMs can be influenced by subtle changes to a wide range of factors such as metal salts, heteroatoms, cations, temperature, pH, rate of addition, sequence of additions, and so on, which may make POM synthesis less reproducible especially when it comes to larger and more complex structures.^[5]

III. Crystallographic studies

According to the single crystal X-ray diffraction data, it seems not all the crystal water and cations can be modeled with accurate location due to the weak diffraction, which is common in POMs. There are some residual disordered or partial-occupied water and cations not located in the cif file, but it will not affect the core structure of POMs. And the final molecular formula was defined by SXRD data combined with the charge balance consideration, elemental analysis and TGA analysis.

Table S1. Charge densities of some representative POM clusters.^[6]

Formula	Anionic charge (-)	# of non-hydrogen atoms	Charge-density ^a
1a	39	239	0.163
2a	42	230	0.183
$[\mathbf{Nb_{13}O_{42}}]$	19	55	0.345
$[\mathbf{Nb_{10}O_{36}}]$	22	46	0.478
	Representative Keg	ggin-type clusters	
$[PM_{12}O_{40}] (M = M_0, W)$	3	53	0.057
$[SiM_{12}O_{40}]$ (M = Mo, W)	4	53	0.075
$[\mathrm{BW}_{12}\mathrm{O}_{40}]$	5	53	0.094
$[\mathbf{CoW_{12}O_{40}}]$	6	53	0.113
$[PNb_{12}O_{40}]$	15	53	0.283
$[SiNb_{12}O_{40}]$	16	53	0.302
	Representative Silve	erton-type clusters	
$[MgW_{12}O_{42}]$	10	55	0.182
$[XMo_{12}O_{42}]$ (X = Ce, Th, U)	8	55	0.145
$[GdMo_{12}O_{42}]$	9	55	0.164
$[NaM_{12}O_{42}] (M = M_0, W)$	11	55	0.2
$[ThNb_{12}O_{42}] \\$	20	55	0.364
$[BaNb_{12}O_{42}]$	22	55	0.4
	Some reported p	olyoxoniobates	
$[Nb_6O_{19}]$	8	25	0.32
$[Ti_2Nb_8O_{28}]$	8	38	0.21
$[\mathbf{Nb_{10}O_{28}}]$	6	38	0.16
$[SiNb_{12}O_{40}]$	16	53	0.30
$[(PO_2)_3PNb_9O_{34}]$	15	53	0.28
$[Si_4Nb_{16}O_{56}]$	16	76	0.21
$[\mathbf{Nb_{27}O_{76}}]$	17	103	0.165
$[\mathbf{Nb_{24}O_{72}}]$	24	96	0.25
$[{ m Nb}_{52}{ m O}_{150}]$	40	202	0.198

^a Charge density = anionic charge / # of non-hydrogen atoms.

Table S2. Crystal data and structure refinement for compounds 1 and 2.

	1	2
empirical formula	$K_{18}Na_{10}H_{141}Te_{16}Nb_{49}O_{239}$	$K_{20}Na_5H_{157}Te_{16}Nb_{46}O_{238}$
FW (g·mol-1)	11494.01	11178.66
temperature (K)	296(2)	296(2)
wavelength (Å)	0.71073	0.71073
cryst syst	Tetragonal	Triclinic
space group	$I^{ar{4}}2d$	p1
a (Å)	29.328(3)	22.5718(14)
b (Å)	29.328(3)	24.9118(15)
c (Å)	28.880(4)	25.0938(15)
α (deg)	90	102.806(2)
β (deg)	90	90.473(2)
γ (deg)	90	92.279(2)
volume (ų)	24840(6)	13746.4(14)
Z	4	2
density calcd (g·cm ⁻³)	3.074	2.701
abs coeff (mm ⁻¹)	4.448	3.922
F(000)	21384.0	10428.0
index ranges	$-34 \le h \le 34$, $-34 \le k \le 34$, $-34 \le l \le 34$	$-30 \le h \le 30$, $-33 \le k \le 33$, $-33 \le l \le 33$
refins collected	216041	167145
indep reflns	10737	66946
GOF on F ²	1.092	1.018
final R indices	$R_I^{\rm a} = 0.0794$	$R_I^{\rm a} = 0.0469$
$[I>=2\sigma(I)]$	$wR_2^b = 0.1962$	$wR_2^b = 0.1212$
R indices (all data)	$R_I^{\rm a} = 0.1118$	$R_I^{\rm a} = 0.0680$
	$wR_2^b = 0.2236$	$wR_2^b = 0.1417$

 $^{{}^{}a}R_{I} = \Sigma ||F_{\theta}| - |F_{c}|| / \Sigma |F_{\theta}|;$ ${}^{b}wR_{2} = \Sigma [w(F_{\theta}^{2} - F_{c}^{2})^{2}] / \Sigma [w(F_{\theta}^{2})^{2}]^{1/2}$

Table S3. Selected bond lengths and angles for compounds 1-2.

	1	2	
Bond type	Bond length (Å)	Bond type	Bond length (Å)
Nb1-O3	2.47(2)	Nb1-O136	1.912(5)
Nb1-O7	1.93(2)	Nb1-O139	2.131(5)
Nb1-O8	1.88(2)	Nb1-O150	2.129(5)
Nb1-O28	1.77(3)	Nb2-O142	1.880(5)
Nb1-O37	2.03(2)	Nb2-O144	2.150(5)
Nb1-O43	2.13(2)	Nb2-O159	2.132(5)
Nb2-O14	2.45(3)	Nb3-O145	1.793(5)
Nb2-O20	1.97(2)	Nb3-O146	1.880(5)
Nb2-O21	1.96(3)	Nb3-O159	2.141(5)
Nb2-O23	2.05(2)	Nb4-O155	1.774(6)
Te1-O9	1.86(2)	Nb5-O56	1.942(5)
Te2-O10	1.85(2)	Te4-O16	2.300(5)
Te2-O16	1.99(2)	Te7-O28	1.862(5)
Te3-O5	1.93(2)	Te13-O143	1.921(5)
Te4-O4	1.94(3)	Te16-O141	1.924(5)
Bond type	Bond angle (deg)	Bond type	Bond angle (deg)
O7-Nb1-O3	83.1(9)	O146-Nb3-O144	91.8(2)
O7-Nb1-O37	152.4(11)	O146-Nb3-O159	94.7(2)
O7-Nb1-O43	82.1(10)	O146-Nb4-O156	168.6(2)
O20-Nb2-O14	87.1(10)	O146-Nb4-O157	87.6(2)
O20-Nb2-O23	158.6(11)	O55-Nb5-O64	82.3(2)
O20-Nb2-O30	83.9(10)	O65-Nb5-O56	97.8(3)
Nb7-O1-Nb8	125.0(13)	O158-Nb7-O139	92.6(2)
Nb3-O2-Nb8	162.6(14)	O158-Nb7-O165	163.8(2)
Nb1-O3-Te1	120.6(11)	O79-Te3-O91	97.1(3)
Te4-O4-Nb11	122.3(13)	O18-Te4-O22	99.3(3)
Nb1-O8-Nb9	123.5(14)	O81-Te5-O94	75.1(3)
Te1-O10-Nb7	133.0(12)	O27-Te7-O32	96.2(3)
Te3-O13-Nb4	97.3(10)	O83-Te8-O95	75.3(3)
Nb9-019-Nb7	143.2(14)	O21-Te13-O23	74.6(3)

Table S4. Comparison of bond lengths and angles between $\{Nb_{13}O_{42}\}$ and Menezesite $\{BaNb_{12}O_{42}\}$.

	${Nb_{13}O_{42}}$	$\{BaNb_{12}O_{42}\}$
	Bond length (Å)	Bond length (Å)
$Nb=O_t$	1.67(3)-1.78(3)	1.851
$Nb-O_{\mathrm{f}}$	2.08(3)-2.25(2)	2.005-2.208
Nb-O _p	1.89(3)- 1.95(3)	1.947
X–O (X = Nb or Ba)	1.97(2)-2.04(3)	2.586
	Bond angle (deg)	Bond angle (deg)
O_t -Nb- O_f	88.1(12)-161.5(11)	92.665-165.37
$Nb-O_f-Nb$	84.9(8)-88.8(10)	87.582-99.322
$Nb-O_p-Nb$	139.4(14)-142.0(15)	134.586
O_p -Nb- O_t	100.4(12)-104.1(13)	98.922
O_p – Nb – O_f	90.2(11)-167.6(10)	82.336-151.379
	$\{Nb_{13}O_{42}\}$	$\{BaNb_{12}O_{42}\}$
Nb…Nb	2.92-2.97	3.056

The terminal Nb=O_t bonds in {Nb₁₃O₄₂} (1.67(3)-1.78(3) Å) are significantly shorter than those in {BaNb₁₂O₄₂} (1.851 Å). In contrast, the bond lengths to the face-sharing oxygen atoms (Nb–O_f) in {Nb₁₃O₄₂} (2.08(3)-2.25(2) Å) fall within a comparable range to those in {BaNb₁₂O₄₂} (2.005-2.208 Å), indicating a similar bonding environment within the face-sharing {Nb₂O₉} units of both structures. Similarly, the peripheral Nb–O_p bond lengths in {Nb₁₃O₄₂} (1.89(3)-1.95(3) Å) align closely with the value observed in {BaNb₁₂O₄₂} (1.947 Å).

A major difference is observed in the bonds connecting the oxygen atoms to the central cation Nb⁵⁺ or Ba²⁺. In {Nb₁₃O₄₂}, this distance is 1.97(2)-2.04(3) Å. The Ba–O length (2.586 Å) is much longer in {BaNb₁₂O₄₂}.

The bond angles further highlight the geometric distortions in $\{Nb_{13}O_{42}\}$ compared to $\{BaNb_{12}O_{42}\}$: The angle across the face-sharing oxygen (O_f) is acuter in $\{Nb_{13}O_{42}\}$ (84.9(8)-88.8(10)°) than in $\{BaNb_{12}O_{42}\}$ (87.582-99.322°), consistent with the shorter Nb···Nb distance. The angle across the peripheral oxygen (O_p) is larger in 1 (139.4(14)-142.0(15)°) than in $\{BaNb_{12}O_{42}\}$ (134.586°), reflecting differences in the corner-sharing linkages between polyhedra. The ranges for O_t -Nb- O_f , O_p -Nb- O_f and O_p -Nb- O_t angles within the niobium coordination sphere are broadly similar.

In summary, while the core bonding parameters related to oxygen (O_f, O_p) are very similar, $\{Nb_{13}O_{42}\}$ exhibits key distinguishing features: (i) significantly shorter terminal Nb=O_t bonds, (ii) a substantially shorter Nb···Nb distance with a acuter Nb-O_f-Nb angle. These analyses suggest that $\{Nb_{13}O_{42}\}$ possesses a more contracted and distorted polyoxoniobate framework compared to $\{BaNb_{12}O_{42}\}$.

Table S5. BVS results of Te atoms and protonated O atoms in polyanion 1a and 2a.

Compound 1					
Atom	Value	Atom	Value	Atom	Value
Te1	4.39	Te2	4.10	Te3	4.08
Te4	3.98	O11	1.40	O28	1.46
O29	1.26	O45	1.46		
Compound 2					
Atom	Value	Atom	Value	Atom	Value
Te1	4.06	Te2	4.05	Te3	4.01
Te4	4.08	Te5	4.09	Te6	4.01
Te7	4.13	Te8	4.09	Te9	4.13
Te10	4.07	Te11	4.03	Te12	4.06
Te13	4.05	Te14	4.06	Te15	4.10
Te16	4.13	O2	1.47	O13	1.47
O30	1.47	O34	1.46	O36	1.49
O37	1.47	O39	1.44	O61	1.47
O63	1.46	O66	1.49	O67	1.45
O68	1.49	O77	1.45	O78	1.47
O87	1.49	O98	1.48	O100	1.48
O106	1.47	O114	1.49	O115	1.42
O118	1.46	O130	1.47	O134	1.39
O140	1.47	O145	1.39	O148	1.34
O154	1.40	O155	1.45	O163	1.38
O164	1.38	O169	1.39		

IV. Detailed views of structures

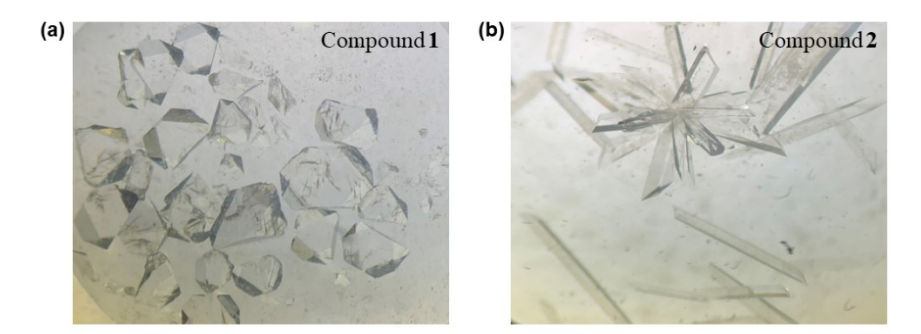


Figure S1. Digital photographs of 1 (a) and 2 (b). The two compounds can be clearly identified by its unique crystal morphology.

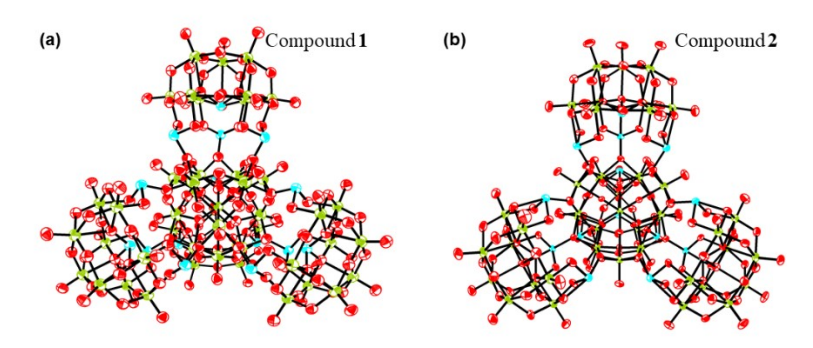


Figure S2. ORTEP drawing of **1** and **2** with thermal ellipsoids at 50% probability. Free water molecules and counter cations are omitted for clarity (Color code: red, O; green, Nb; blue, Te).

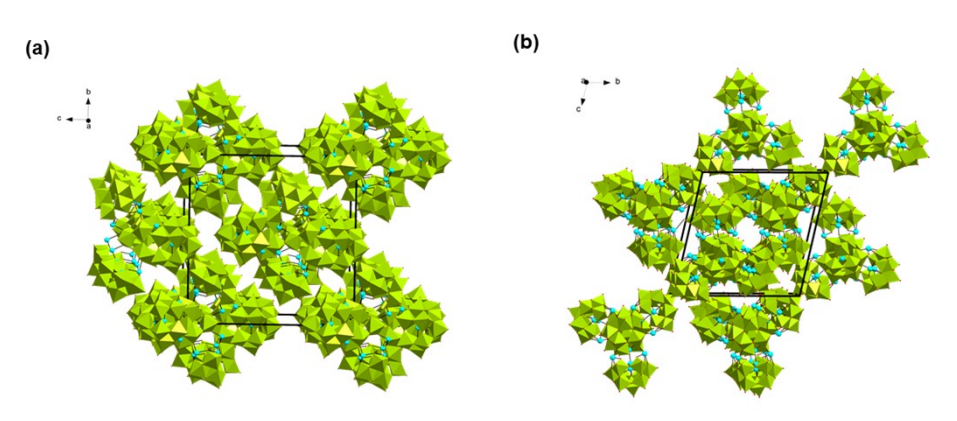


Figure S3. View of the three-dimensional stacking of **1** and **2** along different axis. (a) The polyanion **1a** arrange in the tetragonal space group $I^{\bar{4}}2d$. (b) The lacunary polyanion **2a** arrange in the triclinic space group $P^{\bar{1}}$.

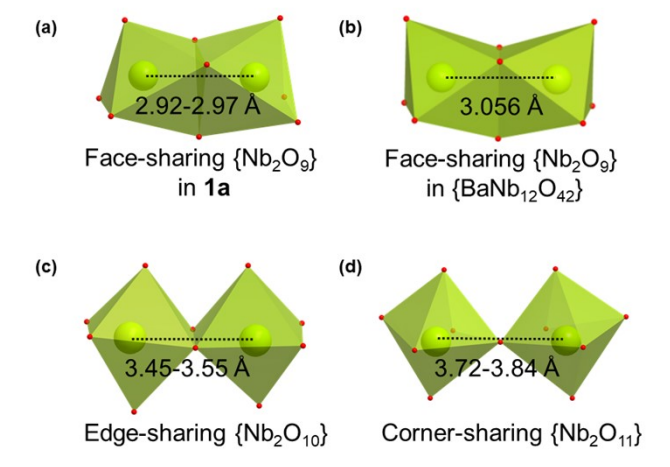


Figure S4. The Nb···Nb distance range of face-sharing $\{Nb_2O_9\}$ in **1a** (a) and in $\{BaNb_{12}O_{42}\}$ (b), edge-sharing $\{Nb_2O_{10}\}$ (c) and corner-sharing $\{Nb_2O_{11}\}$ (d) in **1a**.

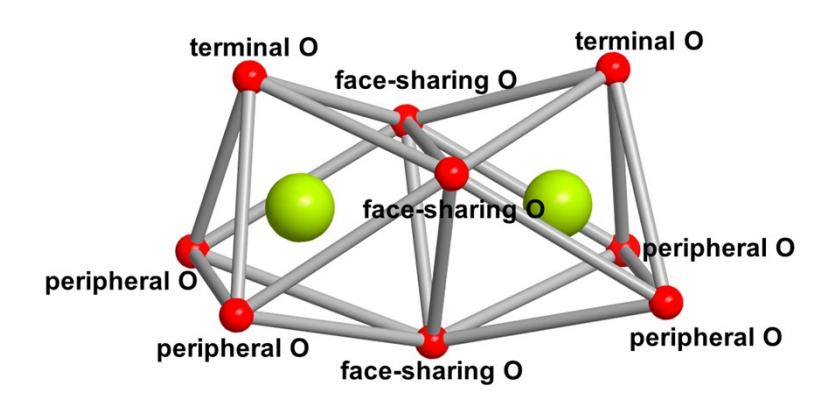


Figure S5. Definition of the O atoms in face-sharing $\{Nb_2O_9\}$.

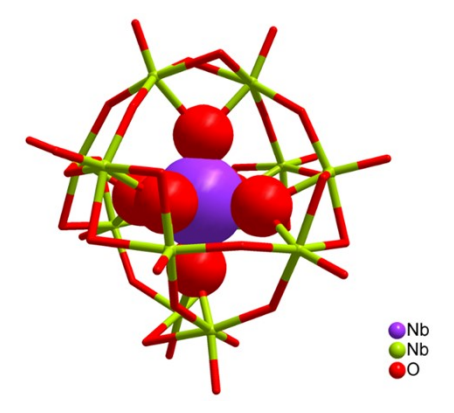


Figure S6. The clathrate structure of $\{Nb_{13}O_{42}\}$ cluster in **1a**. The refinement results for compound **1** reveal that substituting the central NbO_6 with Te^{6+} would lead to high atomic displacement parameters (Ueq = 0.044 Ų for Nb vs. 0.066 Ų for Te model). This indicates poorer fitting to the electron density when modeling Te at this position. An increase in both R_1 (7.83 \rightarrow 7.95) and wR_2 (22.27 \rightarrow 22.41) is observed when the central Nb is substituted with Te.

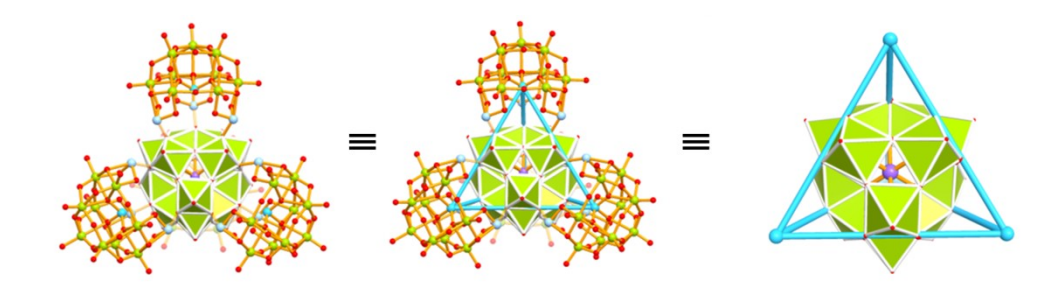


Figure S7. Schematic view of $\{Nb_{13}O_{42}\}$ within a tetrahedron formed by four $\{TeNb_9\}$.

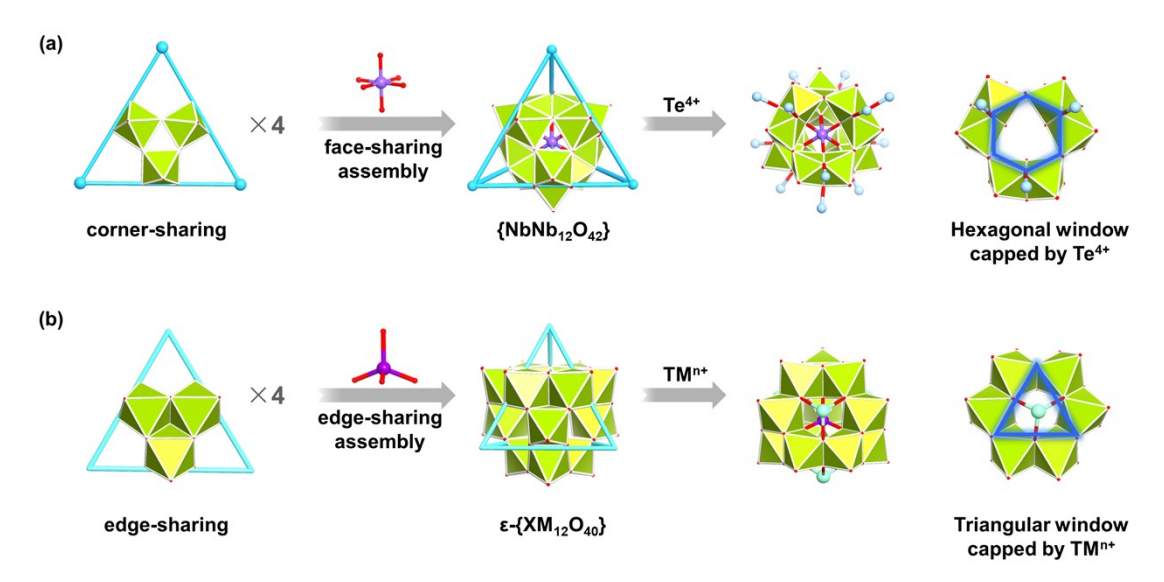


Figure S8. The comparison between $\{Nb_{13}O_{42}\}$ (a) and ϵ -Keggin cluster (b).

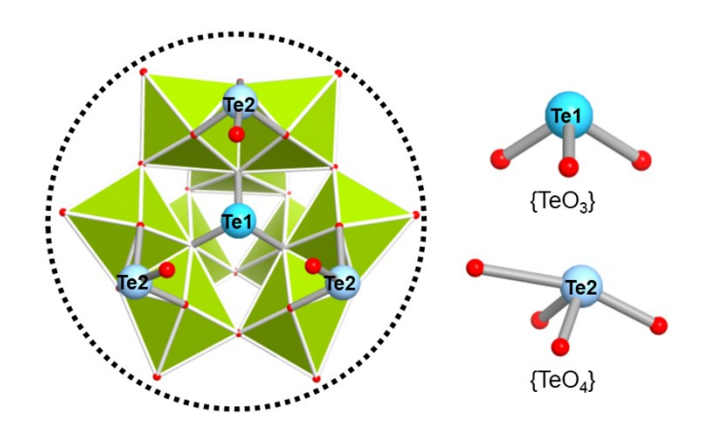


Figure S9. Left: structure representation of $\{(TeO)_3(B-\alpha-TeNb_9O_{33})\}$ unit; Right: coordination geometry of Te in **1a**. Te ions exhibit two distinct coordination modes: three-coordinated Te1 in the lacunary $\{TeNb_9\}$ with a trigonal pyramidal geometry and four-coordinated Te2 surrounding $\{Nb_{13}O_{42}\}$ with a highly distorted "see-saw" geometry.

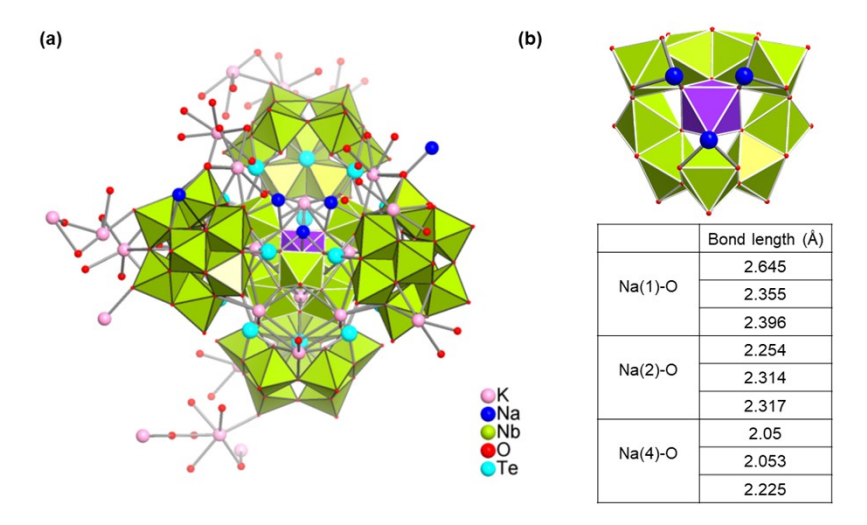


Figure S10. (a) Coordination sites of K^+ and Na^+ in **2a**. (b) Three Na^+ ions occupied the lacunary positions of $\{Nb_{10}O_{36}\}$ and table of Na-O bond length. Some lattice water molecules coordinated with K^+ and Na^+ are not modeled with accurate location due to the distinct diffraction difference between the heavy Nb, Te atoms and light O atoms.

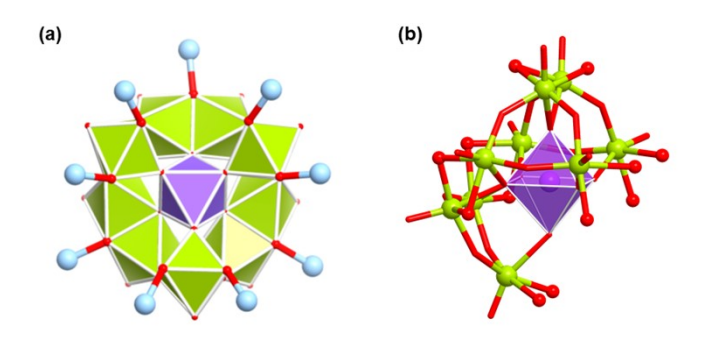


Figure S11. (a) $\{Nb_{10}O_{36}\}$ surrounded by 12 Te(IV); (b) View of the $\{Nb_{10}O_{36}\}$ cluster.

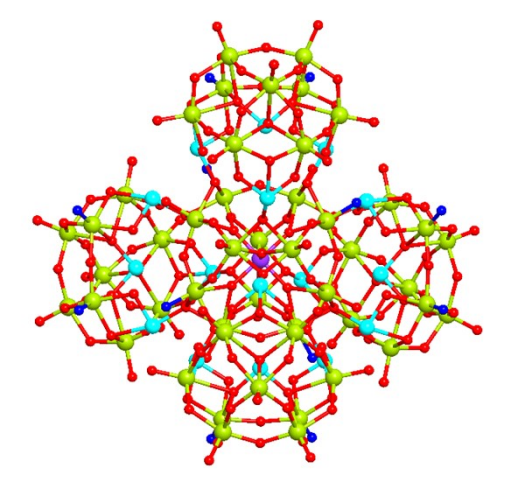


Figure S12. Charge distribution of O atoms in the polyanion **1a**. All alkali metal ions are determined by a combination of X-ray diffractions and elemental analysis. The total negative charge of **1** is -39. Besides the potassium and sodium ions, 11 protons should be added to balance the charges of **1**. Bond valence sum (Σs) reveal that the oxidation states of 158 of 174 O atoms in $K_{18}Na_{10}H_{11}[(Nb_{13}O_{42})\{Te_3(B-\alpha-TeNb_9O_{33})\}_4]\cdot65H_2O$ (**1**) are -2 (-2.30 < Σs < -1.50, marked in red), while the Σs values of 16 O atoms bonded

to Nb have a BVS value of -1.46 - -1.26 (marked in blue), indicating the eleven H⁺ are most likely delocalized on the 16 O atoms. The H⁺ cannot be crystallographically located due to the lack of electron density and inability to interact with X-ray radiation.^[8]

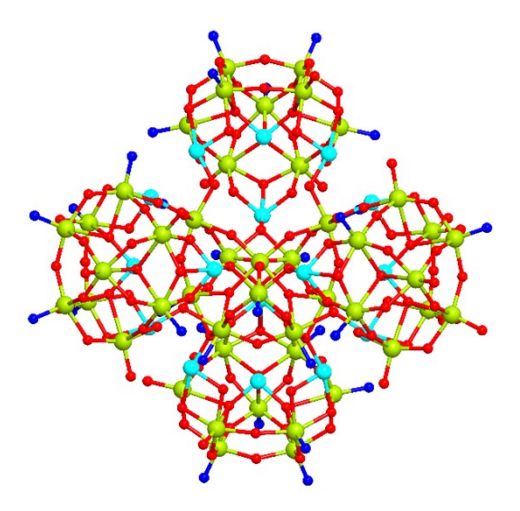


Figure S13. Charge distribution of O atoms in the polyanion **2a**. The total negative charge of **2** is -42. Besides the potassium and sodium ions, 17 protons should be added to balance the charges of **2**. Bond valence sum (Σs) reveal that the oxidation states of 137 of 168 O atoms in $K_{20}Na_5H_{17}[(Nb_{10}O_{36})\{Te_3(B-\alpha-TeNb_9O_{33})\}_4]\cdot70H_2O$ (**2**) are -2 (-2.20 < Σs < -1.50, marked in red). The Σs values of 31 O atoms are in the range of -1.49 – -1.34 (marked in blue), indicating the seventeen H⁺ are most likely delocalized on the 31 O atoms.^[8]

V. Supplementary Physical Characterizations

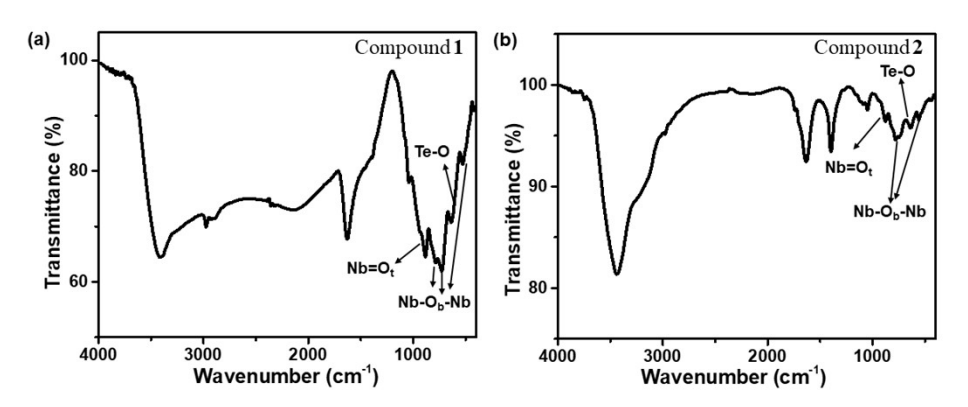


Figure S14. The IR spectra of **1** and **2** recorded between 400 and 4000 cm⁻¹. The terminal Nb=O_t vibrations appear at 887 cm⁻¹ for **1**, and at 872 cm⁻¹ for **2**, respectively. The characteristic peaks at 793, 725, and 532 cm⁻¹ of **1** and 784, 744, and 557 cm⁻¹ of **2** are assigned to the v(Nb-O_b-Nb) stretching vibrations.^[9] The vibration of Te-O is positioned at 636 cm⁻¹.^[10] A peak around 1630 cm⁻¹ can be assigned to H₂O bending mode, which can be seen in all the PONb spectra. The broad bands at around 3406 cm⁻¹ of **1** and 3436 cm⁻¹ of **2** are assigned to the vibration of water molecules.

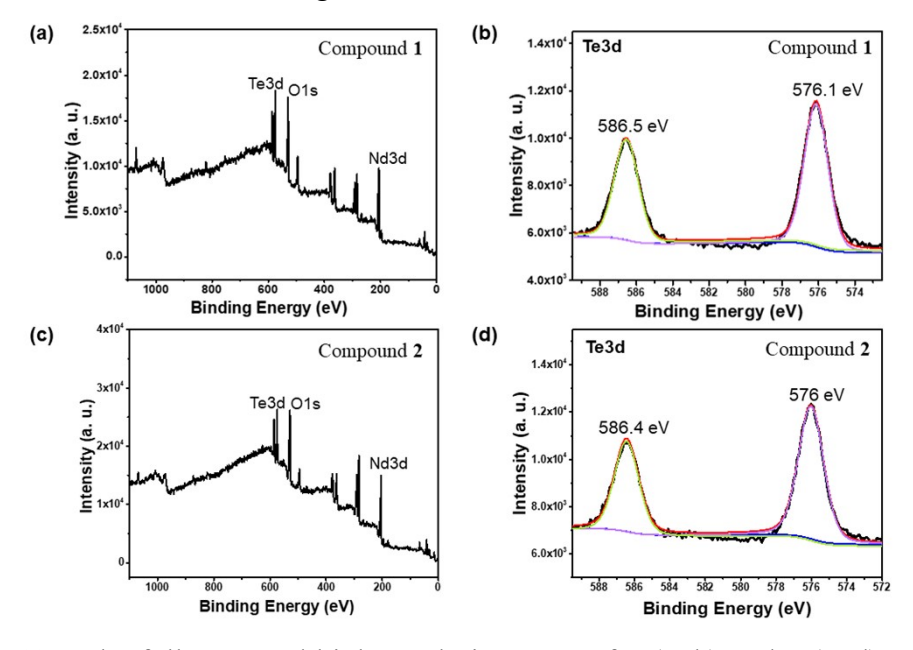


Figure S15. The full-scan and high-resolution XPS of **1** (a, b) and **2** (c, d). The bond valence sum (BVS) calculations (Table S5) and XPS results indicate that the oxidation states of Te in **1** and **2** are all +4. In the Te 3d region, the XPS of **1** gives two peaks at 586.5 and 576.1 eV, which is attributed to Te(IV) $3d_{3/2}$ and Te(IV) $3d_{5/2}$, respectively. The XPS of **2** gives two peaks at 586.4 eV and 576.0 eV, corresponding to Te(IV) $3d_{3/2}$ and Te(IV) $3d_{5/2}$, respectively.

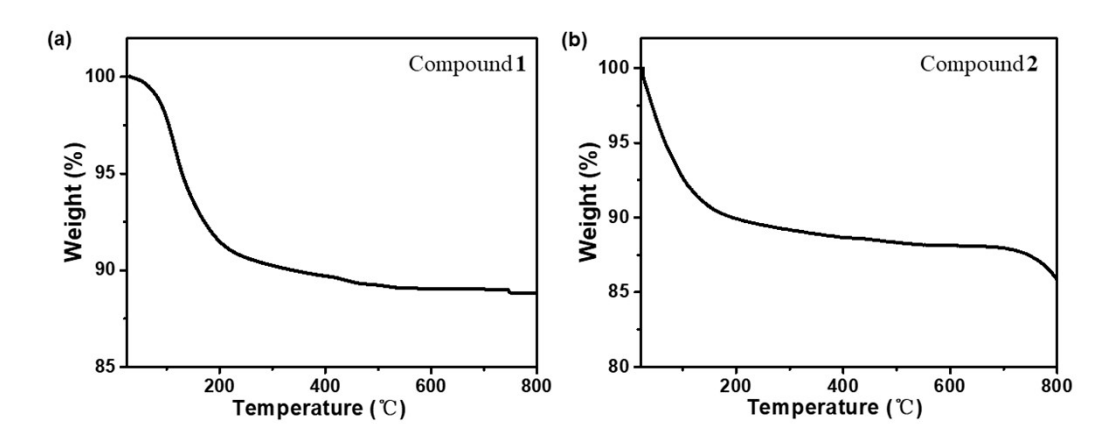


Figure S16. Thermo gravimetric analysis (TGA) of **1** and **2**. The TGA curve of **1** exhibits one slow step of weight loss, giving a total loss of 10.2% (calcd. 10.18%) in the range of 25-200 °C. The weight loss is attributed to the removal of 65 lattice water. Compound **2** undergoes one step of weight loss. The weight loss of 11.43% (calcd. 11.27%) in the range of 25-200 °C is ascribed to the removal of 70 lattice water.

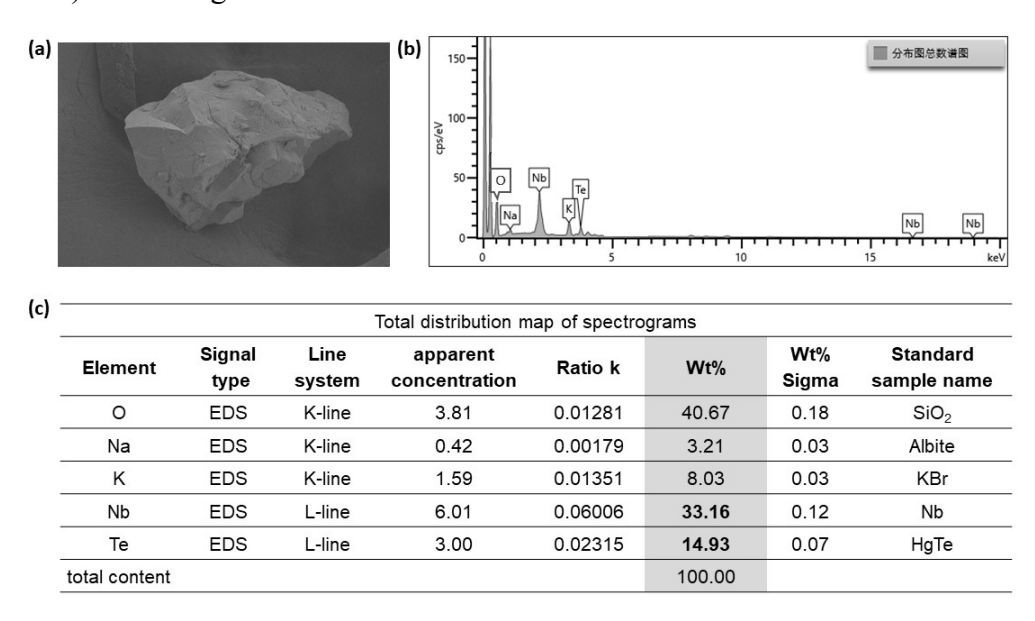


Figure S17. (a) SEM micrograph of compound 1. (b) Analysis spectrum with quantified atomic percentages. (c) EDS quantitative analysis results (wt%).

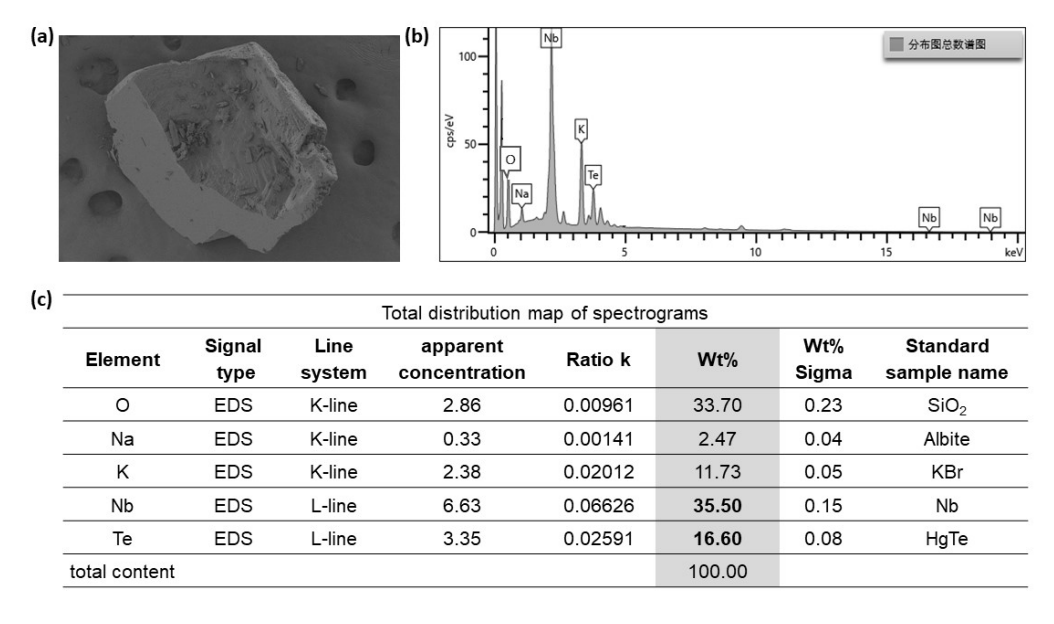


Figure S18. (a) SEM micrograph of compound 2. (b) Analysis spectrum with quantified atomic percentages. (c) EDS quantitative analysis results (wt%).

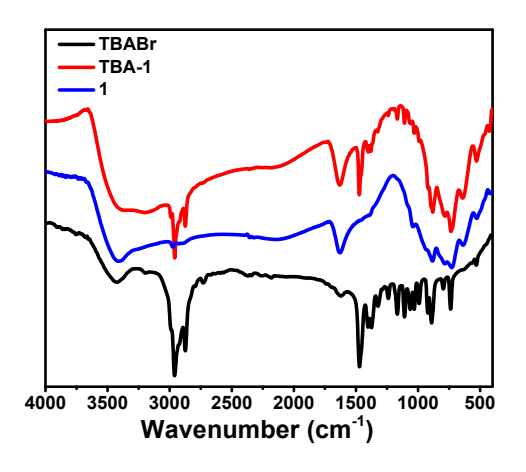


Figure S19. FT-IR spectra of 1, TBA-1, and TBABr.

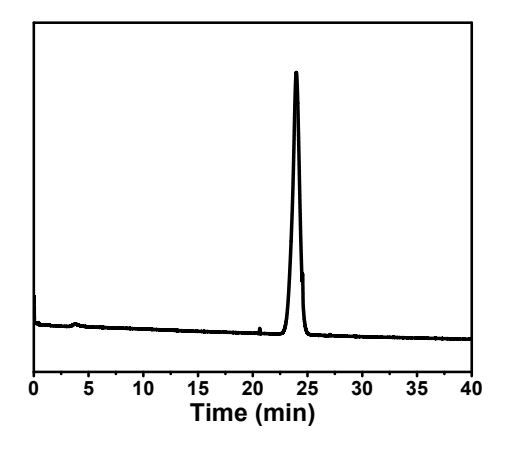


Figure \$20. Electropherogram of 1.

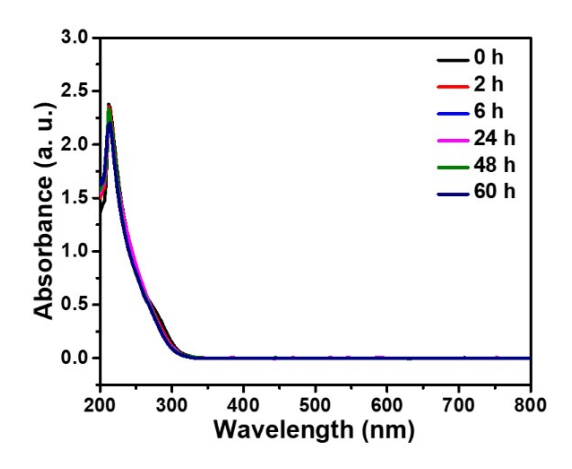


Figure S21. Monitoring of the UV-vis absorption of 1 in aqueous solution for 60 h.

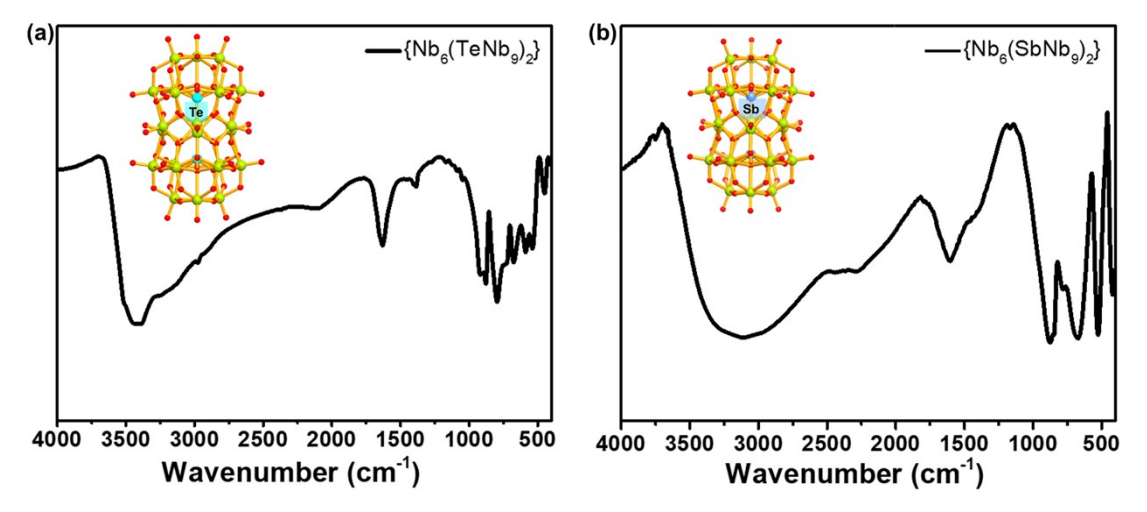


Figure S22. (a) The IR spectra of $\{(NbO)_6(\alpha-TeNb_9O_{33})_2\}$. (b) The IR spectra of the reported sandwich-type $\{(NbO)_6(B-\alpha-SbNb_9O_{33})_2\}$. [11] FT-IR (cm⁻¹): 3140 (s), 1607 (m), 872 (s), 774 (w), 675 (s), 523 (s), 420 (m).

VI. Mass spectrometric study of compounds in water

For 1 and 2, the observed major peaks are very broad (with widths approximately 10 times larger than the simulated peaks). This is generally because of the loss of weakly associated solvent molecules or cation exchange, which is a common issue for high nuclearity and charge of POM species. In these cases, an m/z value is assigned based on the most intense peak found at near the center of an estimated Gaussian distribution. Each major "peak" comprising the "true" isotopic envelope is assigned in the following. The characteristic m/z within the peak envelopes can be observed as shown in the following figures. Expansion of any peak clearly reveals the m/z pattern.

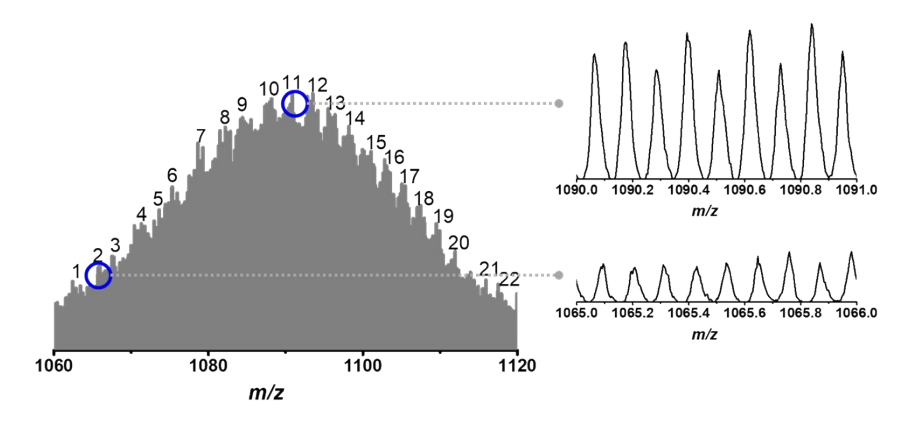


Figure S23. The ESI mass spectrum of compound 1 around m/z 1090.84.

Table S6. Detailed assignment for compound 1 around m/z 1090.84.

Peak number	m/z observed	Assignment	m/z calculated
1	1062.43	$[KNa_{5}H_{24}(Nb_{13}O_{42})\{Te_{3}(B-\alpha-TeNb_{9}O_{33})\}_{4}]^{9\text{-}}$	1062.01
2	1065.76	$[K_3Na_3H_{24}(Nb_{13}O_{42})\{Te_3(B-\alpha\text{-}TeNb_9O_{33})\}_4]^{9\text{-}}$	1065.56
3	1067.53	$[K_4Na_2H_{24}(Nb_{13}O_{42})\{Te_3(B\text{-}\alpha\text{-}TeNb_9O_{33})\}_4]^{9\text{-}}$	1067.34
4	1071.31	$[K_5Na_2H_{23}(Nb_{13}O_{42})\{Te_3(B-\alpha\text{-}TeNb_9O_{33})\}_4]^{9\text{-}}$	1071.55
5	1073.63	$[K_2Na_8H_{20}(Nb_{13}O_{42})\{Te_3(B\text{-}\alpha\text{-}TeNb_9O_{33})\}_4]^{9\text{-}}$	1073.56
6	1075.30	$[K_3Na_7H_{20}(Nb_{13}O_{42})\{Te_3(B-\alpha\text{-}TeNb_9O_{33})\}_4]^{9\text{-}}$	1075.33
7	1078.63	$[K_2Na_{10}H_{18}(Nb_{13}O_{42})\{Te_3(B\hbox{-}\alpha\hbox{-}TeNb_9O_{33})\}_4]^{9\hbox{-}}$	1078.44
8	1082.18	$[K_7Na_3H_{20}(Nb_{13}O_{42})\{Te_3(B-\alpha\text{-}TeNb_9O_{33})\}_4]^{9\text{-}}$	1082.43
9	1084.40	$[K_4Na_9H_{17}(Nb_{13}O_{42})\{Te_3(B\text{-}\alpha\text{-}TeNb_9O_{33})\}_4]^{9\text{-}}$	1084.43
10	1088.18	$[K_2Na_{14}H_{14}(Nb_{13}O_{42})\{Te_3(B\hbox{-}\alpha\hbox{-}TeNb_9O_{33})\}_4]^{9\hbox{-}}$	1088.21
11	1090.84	$[K_9Na_3H_{18}(Nb_{13}O_{42})\{Te_3(B\text{-}\alpha\text{-}TeNb_9O_{33})\}_4]^{9\text{-}}$	1090.87
12	1093.50	$[K_5Na_{11}H_{14}(Nb_{13}O_{42})\{Te_3(B\hbox{-}\alpha\hbox{-}TeNb_9O_{33})\}_4]^{9\hbox{-}}$	1093.54
13	1095.50	$[K_2Na_{17}H_{11}(Nb_{13}O_{42})\{Te_3(B\hbox{-}\alpha\hbox{-}TeNb_9O_{33})\}_4]^{9\hbox{-}}$	1095.54
14	1098.17	$[K_9Na_6H_{15}(Nb_{13}O_{42})\{Te_3(B-\alpha\text{-}TeNb_9O_{33})\}_4]^{9\text{-}}$	1098.19
15	1101.05	$[K_{12}Na_2H_{16}(Nb_{13}O_{42})\{Te_3(B\hbox{-}\alpha\hbox{-}TeNb_9O_{33})\}_4]^{9\hbox{-}}$	1101.08
16	1102.83	$[K_{13}NaH_{16}(Nb_{13}O_{42})\{Te_3(B\text{-}\alpha\text{-}TeNb_9O_{33})\}_4]^{9\text{-}}$	1102.85
17	1104.82	$[K_{10}Na_7H_{13}(Nb_{13}O_{42})\{Te_3(B\text{-}\alpha\text{-}TeNb_9O_{33})\}_4]^{9\text{-}}$	1104.85
18	1107.49	$[K_6Na_{15}H_9(Nb_{13}O_{42})\{Te_3(B-\alpha\text{-}TeNb_9O_{33})\}_4]^{9\text{-}}$	1107.52
19	1109.49	$[K_{14}Na_2H_{14}(Nb_{13}O_{42})\{Te_3(B\hbox{-}\alpha\hbox{-}TeNb_9O_{33})\}_4]^{9\hbox{-}}$	1109.51
20	1111.94	$[K_{14}Na_3H_{13}(Nb_{13}O_{42})\{Te_3(B\text{-}\alpha\text{-}TeNb_9O_{33})\}_4]^{9\text{-}}$	1111.95
21	1115.92	$[K_8Na_5H_{17}(Nb_{13}O_{42})\{Te_3(B\text{-}\alpha\text{-}TeNb_9O_{33})\}_4]^{9\text{-}}$	1115.96

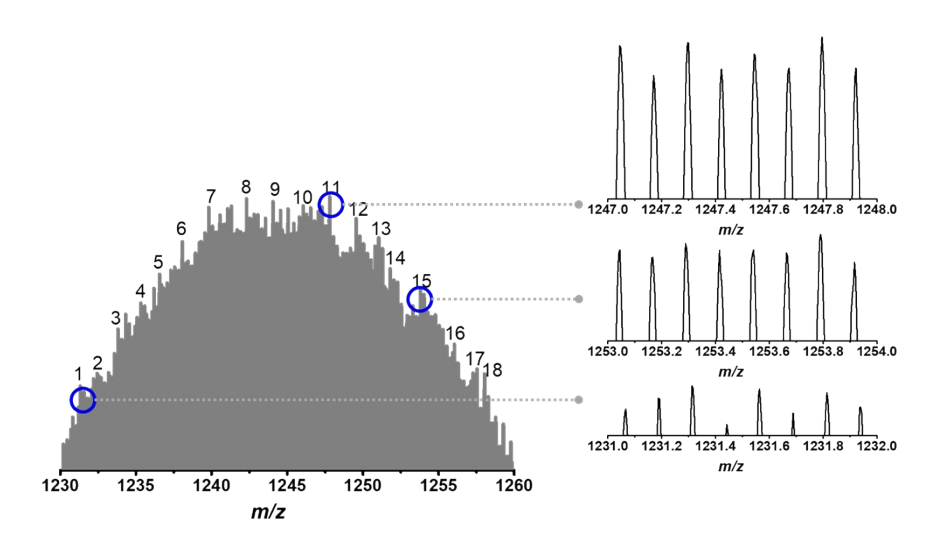


Figure S24. The ESI mass spectrum of compound 1 around m/z 1247.80.

Table S7. Detailed assignment for compound 1 around m/z 1247.80.

Peak number	m/z observed	Assignment	m/z calculated
1	1231.31	$[K_{11}NaH_{19}(Nb_{13}O_{42})\{Te_3(B\text{-}\alpha\text{-}TeNb_9O_{33})\}_4]^{8\text{-}}$	1231.34
2	1232.44	$[K_6Na_{10}H_{15}(Nb_{13}O_{42})\{Te_3(B\hbox{-}\alpha\hbox{-}TeNb_9O_{33})\}_4]^{8\hbox{-}}$	1232.35
3	1232.81	$[K_3Na_{15}H_{13}(Nb_{13}O_{42})\{Te_3(B\hbox{-}\alpha\hbox{-}TeNb_9O_{33})\}_4]^{8\hbox{-}}$	1231.86
4	1235.31	$[K_2Na_{18}H_{11}(Nb_{13}O_{42})\{Te_3(B\hbox{-}\alpha\hbox{-}TeNb_9O_{33})\}_4]^{8\hbox{-}}$	1235.35
5	1236.56	$[K_4Na_{15}H_{12}(Nb_{13}O_{42})\{Te_3(B\hbox{-}\alpha\hbox{-}TeNb_9O_{33})\}_4]^{8\hbox{-}}$	1236.60
6	1238.06	$[K_9Na_7H_{15}(Nb_{13}O_{42})\{Te_3(B-\alpha\text{-}TeNb_9O_{33})\}_4]^{8\text{-}}$	1238.34
7	1239.80	$[K_7Na_{11}H_{13}(Nb_{13}O_{42})\{Te_3(B\hbox{-}\alpha\hbox{-}TeNb_9O_{33})\}_4]^{8\hbox{-}}$	1239.84
8	1242.30	$[K_{11}Na_5H_{15}(Nb_{13}O_{42})\{Te_3(B\hbox{-}\alpha\hbox{-}TeNb_9O_{33})\}_4]^{8\hbox{-}}$	1242.33
9	1244.05	$[K_5Na_{16}H_{10}(Nb_{13}O_{42})\{Te_3(B\hbox{-}\alpha\hbox{-}TeNb_9O_{33})\}_4]^{8\hbox{-}}$	1244.09
10	1245.05	$[K_{11}Na_6H_{14}(Nb_{13}O_{42})\{Te_3(B\hbox{-}\alpha\hbox{-}TeNb_9O_{33})\}_4]^{8\hbox{-}}$	1245.08
11	1247.80	$[K_{11}Na_7H_{13}(Nb_{13}O_{42})\{Te_3(B\hbox{-}\alpha\hbox{-}TeNb_9O_{33})\}_4]^{8\hbox{-}}$	1247.83
12	1249.55	$[K_5Na_{18}H_8(Nb_{13}O_{42})\{Te_3(B\text{-}\alpha\text{-}TeNb_9O_{33})\}_4]^{8\text{-}}$	1249.59
13	1251.04	$[K_{14}Na_3H_{14}(Nb_{13}O_{42})\{Te_3(B\hbox{-}\alpha\hbox{-}TeNb_9O_{33})\}_4]^{8\hbox{-}}$	1251.07
14	1251.79	$[K_{13}Na_5H_{13}(Nb_{13}O_{42})\{Te_3(B\hbox{-}\alpha\hbox{-}TeNb_9O_{33})\}_4]^{8\hbox{-}}$	1251.82
15	1253.79	$[K_{14}Na_4H_{13}(Nb_{13}O_{42})\{Te_3(B\hbox{-}\alpha\hbox{-}TeNb_9O_{33})\}_4]^{8\hbox{-}}$	1253.82
16	1256.04	$[K_{11}Na_{10}H_{10}(Nb_{13}O_{42})\{Te_3(B\text{-}\alpha\text{-}TeNb_9O_{33})\}_4]^{8\text{-}}$	1256.07
17	1257.54	$[K_9Na_{14}H_8(Nb_{13}O_{42})\{Te_3(B\text{-}\alpha\text{-}TeNb_9O_{33})\}_4]^{8\text{-}}$	1257.58
18	1258.03	$[K_{16}Na_2H_{13}(Nb_{13}O_{42})\{Te_3(B\hbox{-}\alpha\hbox{-}TeNb_9O_{33})\}_4]^{8\hbox{-}}$	1258.06

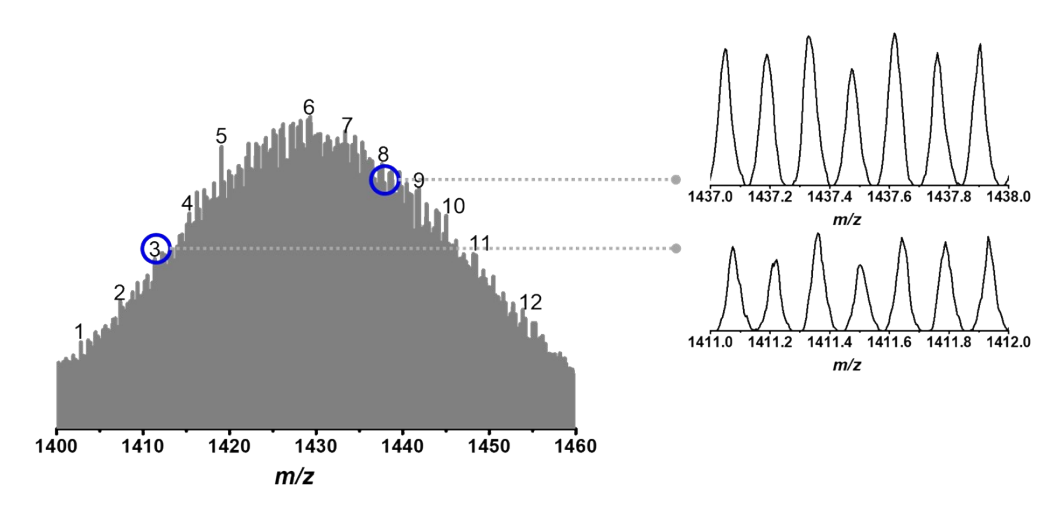


Figure S25. The ESI mass spectrum of compound 1 around m/z 1429.33.

Table S8. Detailed assignment for compound 1 around m/z 1429.33.

Peak number	m/z observed	Assignment	m/z calculated
1	1402.80	$[K_9Na_3H_{20}(Nb_{13}O_{42})\{Te_3(B-\alpha\text{-}TeNb_9O_{33})\}_4]^{7\text{-}}$	1402.83
2	1407.36	$[K_{11}NaH_{20}(Nb_{13}O_{42})\{Te_3(B\text{-}\alpha\text{-}TeNb_9O_{33})\}_4]^{7\text{-}}$	1407.39
3	1411.36	$[K_{10}Na_4H_{18}(Nb_{13}O_{42})\{Te_3(B\text{-}\alpha\text{-}TeNb_9O_{33})\}_4]^{7\text{-}}$	1411.39
4	1415.35	$[K_9Na_7H_{16}(Nb_{13}O_{42})\{Te_3(B\text{-}\alpha\text{-}TeNb_9O_{33})\}_4]^{7\text{-}}$	1415.39
5	1419.07	$[K_{12}Na_3H_{17}(Nb_{13}O_{42})\{Te_3(B\text{-}\alpha\text{-}TeNb_9O_{33})\}_4]^{7\text{-}}$	1419.10
6	1429.33	$[K_{11}Na_8H_{13}(Nb_{13}O_{42})\{Te_3(B\text{-}\alpha\text{-}TeNb_9O_{33})\}_4]^{7\text{-}}$	1429.38
7	1433.33	$[K_{10}Na_{11}H_{11}(Nb_{13}O_{42})\{Te_3(B\text{-}\alpha\text{-}TeNb_9O_{33})\}_4]^{7\text{-}}$	1433.37
8	1437.62	$[K_{16}Na_2H_{14}(Nb_{13}O_{42})\{Te_3(B\text{-}\alpha\text{-}TeNb_9O_{33})\}_4]^{7\text{-}}$	1437.93
9	1441.90	$[K_{11}Na_{12}H_9(Nb_{13}O_{42})\{Te_3(B\text{-}\alpha\text{-}TeNb_9O_{33})\}_4]^{7\text{-}}$	1441.94
10	1445.04	$[K_{11}Na_{13}H_8(Nb_{13}O_{42})\{Te_3(B\text{-}\alpha\text{-}TeNb_9O_{33})\}_4]^{7\text{-}}$	1445.08
11	1448.18	$[K_{11}Na_{14}H_7(Nb_{13}O_{42})\{Te_3(B\text{-}\alpha\text{-}TeNb_9O_{33})\}_4]^{7\text{-}}$	1448.22
12	1453.89	$[K_{12}Na_{14}H_6(Nb_{13}O_{42})\{Te_3(B\text{-}\alpha\text{-}TeNb_9O_{33})\}_4]^{7\text{-}}$	1453.64

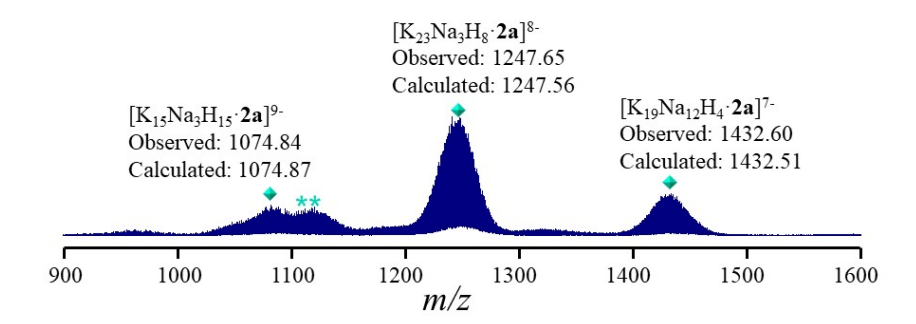


Figure S26. Negative mode mass spectrum of compound **2** in the m/z range of 900-1600. Three main peaks can be ascribed to the parent skeleton of $\{(Nb_{10}O_{36})[Te_3(B-\alpha-TeNb_9O_{33})]_4\}$ (**2a**) encompassing different combinations of H⁺, Na⁺, K⁺. An extra peak located at around 1120 m/z (highlighted by the asterisk) corresponds to $\{(Nb_{10}O_{36})[Te_3(B-\alpha-TeNb_9O_{33})]_3\}$ where a supporting ligand $\{Te_3(B-\alpha-TeNb_9O_{33})\}$ fall off from the parent cluster **2a** in ESI process. The results show that the lacunary

cluster 2a is less stable than the plenary 1a in solution. Besides, the detection of the extra peak largely confirms our hypothesis that the supporting ligand $\{Te_3(B-\alpha-TeNb_9O_{33})\}$ generated *in situ* is necessary module in the self-assembly of 1 and 2. Full spectral assignments are provided in the following.

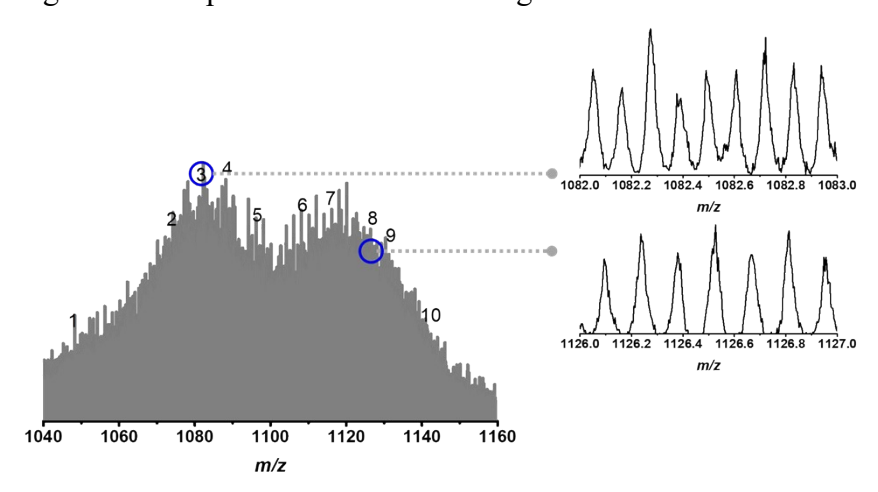


Figure S27. The ESI mass spectrum of compound **2** around m/z 1096.26.

Table S9. Detailed assignment for compound 2 around m/z 1096.26.

Peak number	m/z observed	Assignment	m/z calculated
1	1048.31	$[K_7Na_6H_{20}(Nb_{10}O_{36})\{Te_3(B\hbox{-}\alpha\hbox{-}TeNb_9O_{33})\}_4]^{9\hbox{-}}$	1048.46
2	1074.84	$[K_{15}Na_3H_{15}(Nb_{10}O_{36})\{Te_3(B-\alpha\text{-}TeNb_9O_{33})\}_4]^{9\text{-}}$	1074.87
3	1082.49	$[K_{15}Na_6H_{12}(Nb_{10}O_{36})\{Te_3(B-\alpha\text{-}TeNb_9O_{33})\}_4]^{9\text{-}}$	1082.20
4	1088.38	$[K_{17}Na_5H_{11}(Nb_{10}O_{36})\{Te_3(B\hbox{-}\alpha\hbox{-}TeNb_9O_{33})\}_4]^{9\hbox{-}}$	1088.42
5	1096.26	$[K_{20}Na_3H_{10}(Nb_{10}O_{36})\{Te_3(B\hbox{-}\alpha\hbox{-}TeNb_9O_{33})\}_4]^{9\hbox{-}}$	1096.18
6	**1108.69	$[K_{14}Na_3H_{13}(Nb_{10}O_{36})\{Te_3(B\hbox{-}\alpha\hbox{-}TeNb_9O_{33})\}_3]^{7\hbox{-}}$	1108.47
7	**1116.39	$[K_{16}Na_2H_{12}(Nb_{10}O_{36})\{Te_3(B\hbox{-}\alpha\hbox{-}TeNb_9O_{33})\}_3]^{7\hbox{-}}$	1116.17
8	**1126.67	$[K_{15}Na_7H_8(Nb_{10}O_{36})\{Te_3(B\text{-}\alpha\text{-}TeNb_9O_{33})\}_3]^{7\text{-}}$	1126.45
9	**1130.52	$[K_{14}Na_{10}H_6(Nb_{10}O_{36})\{Te_3(B\hbox{-}\alpha\hbox{-}TeNb_9O_{33})\}_3]^{7\hbox{-}}$	1130.45
10	**1141.51	$[K_{16}Na_{10}H_4(Nb_{10}O_{36})\{Te_3(B\text{-}\alpha\text{-}TeNb_9O_{33})\}_3]^{7\text{-}}$	1141.29

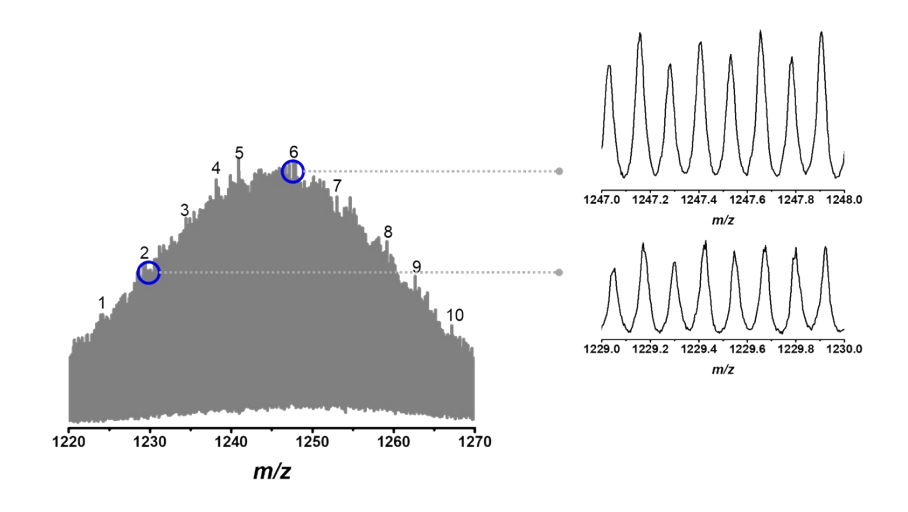


Figure S28. The ESI mass spectrum of compound 2 around m/z 1247.65.

Table S10. Detailed assignment for compound 2 around m/z 1247.65.

Peak number	m/z observed	Assignment	m/z calculated
1	1223.93	$[K_{14}Na_{10}H_{10}(Nb_{10}O_{36})\{Te_3(B-\alpha\text{-}TeNb_9O_{33})\}_4]^{8\text{-}}$	1223.85
2	1229.43	$[K_{18}Na_5H_{11}(Nb_{10}O_{36})\{Te_3(B\text{-}\alpha\text{-}TeNb_9O_{33})\}_4]^{8\text{-}}$	1229.34
3	1234.42	$[K_{11}Na_{19}H_4(Nb_{10}O_{36})\{Te_3(B\hbox{-}\alpha\hbox{-}TeNb_9O_{33})\}_4]^{8\hbox{-}}$	1234.34
4	1238.16	$[K_{21}Na_3H_{10}(Nb_{10}O_{36})\{Te_3(B\hbox{-}\alpha\hbox{-}TeNb_9O_{33})\}_4]^{8\hbox{-}}$	1238.08
5	1240.91	$[K_{21}Na_4H_9(Nb_{10}O_{36})\{Te_3(B\text{-}\alpha\text{-}TeNb_9O_{33})\}_4]^{8\text{-}}$	1240.82
6	1247.65	$[K_{23}Na_3H_8(Nb_{10}O_{36})\{Te_3(B\text{-}\alpha\text{-}TeNb_9O_{33})\}_4]^{8\text{-}}$	1247.56
7	1252.28	$[K_{24}Na_3H_7(Nb_{10}O_{36})\{Te_3(B\text{-}\alpha\text{-}TeNb_9O_{33})\}_4]^{8\text{-}}$	1252.31
8	1259.14	$[K_{26}Na_2H_6(Nb_{10}O_{36})\{Te_3(B\text{-}\alpha\text{-}TeNb_9O_{33})\}_4]^{8\text{-}}$	1259.05
9	1262.65	$[K_{25}Na_5H_4(Nb_{10}O_{36})\{Te_3(B\text{-}\alpha\text{-}TeNb_9O_{33})\}_4]^{8\text{-}}$	1262.55
10	1267.14	$[K_{26}Na_5H_3(Nb_{10}O_{36})\{Te_3(B\text{-}\alpha\text{-}TeNb_9O_{33})\}_4]^{8\text{-}}$	1267.29

3 1432.0 1432.2 1432.4 1432.6 1432.8 1433.0 m/z 1417.0 1417.2 1417.4 1417.8 1418.0 m/z 1400 1410 1420 1430 1440 1450 1460 m/z

Figure S29. The ESI mass spectrum of compound **2** around m/z 1432.60.

Table S11. Detailed assignment for compound **2** around m/z 1432.60.

Peak number	m/z observed	Assignment	m/z calculated
1	1412.63	$[K_{20}Na_4H_{11}(Nb_{10}O_{36})\{Te_3(B-\alpha\text{-}TeNb_9O_{33})\}_4]^{7\text{-}}$	1412.81
2	1417.76	$[K_{18}Na_9H_8(Nb_{10}O_{36})\{Te_3(B\hbox{-}\alpha\hbox{-}TeNb_9O_{33})\}_4]^{7\hbox{-}}$	1417.66
3	1423.46	$[K_{22}Na_4H_9(Nb_{10}O_{36})\{Te_3(B\hbox{-}\alpha\hbox{-}TeNb_9O_{33})\}_4]^{7\hbox{-}}$	1423.65
4	1432.60	$[K_{19}Na_{12}H_4(Nb_{10}O_{36})\{Te_3(B\text{-}\alpha\text{-}TeNb_9O_{33})\}_4]^{7\text{-}}$	1432.51
5	1437.74	$[K_{24}Na_5H_6(Nb_{10}O_{36})\{Te_3(B-\alpha\text{-}TeNb_9O_{33})\}_4]^{7\text{-}}$	1437.63
6	1442.02	$[K_{26}Na_3H_6(Nb_{10}O_{36})\{Te_3(B\text{-}\alpha\text{-}TeNb_9O_{33})\}_4]^{7\text{-}}$	1442.20
7	1446.31	$[K_{25}Na_6H_4(Nb_{10}O_{36})\{Te_3(B\text{-}\alpha\text{-}TeNb_9O_{33})\}_4]^{7\text{-}}$	1446.20
8	1449.73	$[K_{28}Na_2H_5(Nb_{10}O_{36})\{Te_3(B\text{-}\alpha\text{-}TeNb_9O_{33})\}_4]^{7\text{-}}$	1449.90
9	1453.44	$[K_{24}Na_{10}H(Nb_{10}O_{36})\{Te_3(B\text{-}\alpha\text{-}TeNb_9O_{33})\}_4]^{7\text{-}}$	1453.34
10	1457.73	$[K_{30}NaH_4(Nb_{10}O_{36})\{Te_3(B\text{-}\alpha\text{-}TeNb_9O_{33})\}_4]^{7\text{-}}$	1457.61

VII. The computing method for volume fractions of different PONb species in solution

The fitting is performed using the Oligomer in the ATSAS package. [12] The input experimental SAXS curve data contributed from a mixture of several species is written as $I(q) = \sum V_i I_i(q)$, where V_i and $I_i(q)$ are the volume fraction and theoretical scattering intensity of the i-th specy, respectively. The scattering intensity (form factor) of each species we using in the fitting is calculated from the corresponding cif file through Crysol, which is also in the ATSAS package. In this case, four candidate species — TeNb₉, Nb₁₃O₄₂, Nb₆(TeNb₉)₂ and 1a — were selected for the fitting model due to their potential presence in solution. The scattering intensity I(q) was expressed as: $I(q) = V_I I(\text{TeNb}_9) + V_2 I(\text{Nb}_{13}\text{O}_{42}) + V_3 I(\text{Nb}_6(\text{TeNb}_9)_2) + V_4 I(\text{1a})$. With the input theoretical scattering intensity, the volume fraction is found by solving a system of linear functions using the algorithm of non-negative least square to minimize the deviation of calculated scattering curve from

experimental scattering curve.

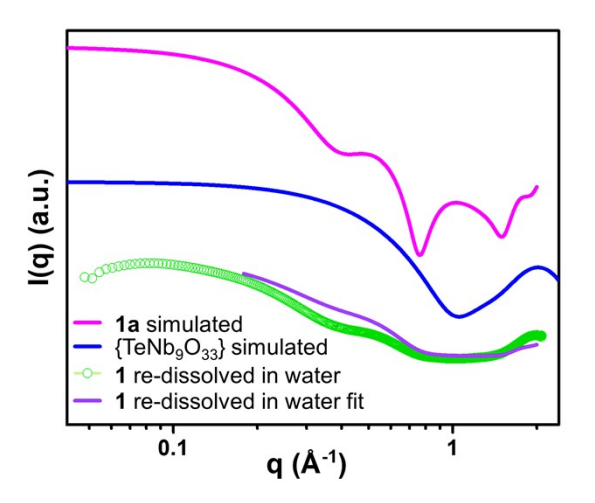


Figure S30. SAXS data for 1 re-dissolved in water (green) and fitting curve (purple).

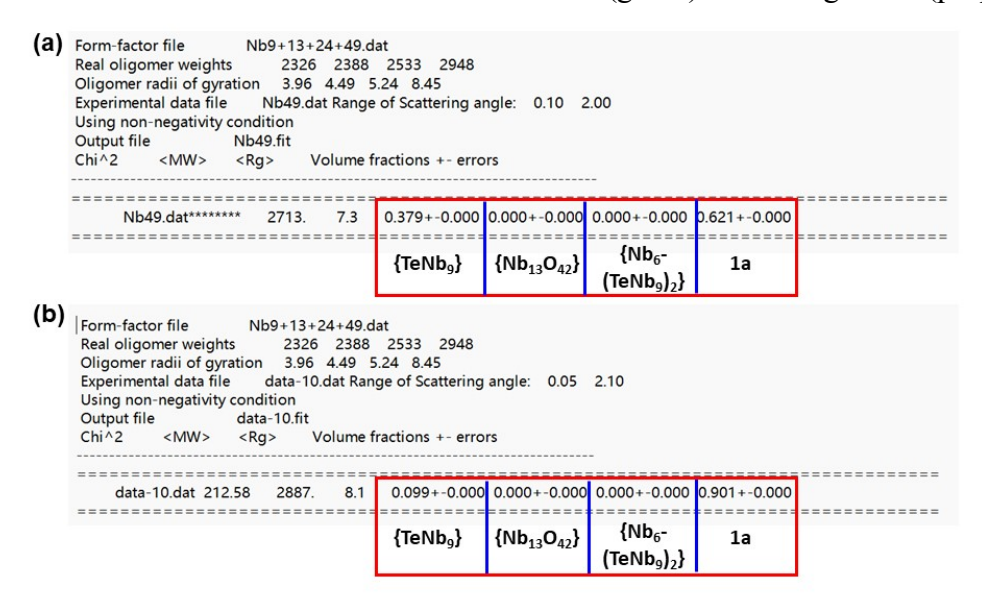


Figure S31. Screenshot of fitting result for 1 re-dissolved in water (a) and 0.05 M pH = $10.00 \text{ Na}_2\text{CO}_3$ -NaHCO₃ buffer solution (b). The results are highlighted by red boxes and represents the volume fraction of $\{\text{TeNb}_9\}$, $\{\text{Nb}_{13}\text{O}_{42}\}$, $\{\text{Nb}_6(\text{TeNb}_9)_2\}$ and 1a, respectively.

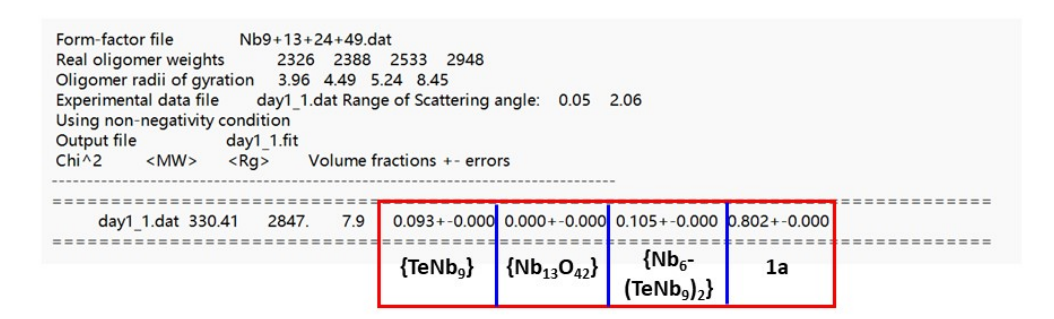


Figure S32. Screenshot of fitting result for fresh reaction solution of compound **1** after hydrothermal treatment.

VIII. Computational details, EDA analysis, and frontier molecular orbitals of different PONb species

A comparison of Nb-Nb bond lengths $\{Nb_2O_9\}$ was carried out between the experimental structures and optimized structures with different methods, which shows that the results obtained by the $MN15^{[13]}$ descripts better. Therefore, all following ground-state geometry optimizations of $\{Nb_2O_9\}$, $\{Nb_2O_{10}\}$, $\{Nb_2O_{11}\}$ and $\{(TeO_3)_2Nb_2O_9\}$ were carried out at the $SMD^{[14]}(H_2O)/MN15/def2-TZVPP^{[15]}$ level.

Table S12. Nb-Nb bond lengths of $\{Nb_2O_9\}$ optimized under different functionals at SMD $(H_2O)/(U)DFT/def2$ -TZVPP level.

Method	Nb-Nb bond length (Å)	
{Nb ₂ O ₉ } (EXP.)	2.985	
B3LYP-D3	3.075	
B3PW91	3.042	
M06-2X	3.092	
MN15	3.031	
PBE	3.070	
WB97XD	3.072	

The Energy Decomposition Analysis (EDA^[16]) was carried out at the def2-TZVPP^[15] basis sets. All of the above calculations were performed with Gaussian 16 program^[17].

The bonding analysis between the Nb atoms (A) and O atoms (B) in a molecule (AB) was explored by EDA. In EDA calculations, the molecule AB devides into two fragments A and B. The physical nature of the interaction is derived by the decomposition of the instantaneous interaction energy. The EDA approach decomposes the instantaneous interaction energy ΔE_{int} of A-B bond into four parts:

$$\Delta E_{\text{int}} = \Delta E_{\text{els}} + \Delta E_{\text{xrep}} + \Delta E_{\text{orb}} + \Delta E_{\text{c}}$$

The attractive $\Delta E_{\rm els}$ indicates the quasi-classical electrostatics interaction between the prepared fragments A and B. The second term $\Delta E_{\rm xrep}$ is exchange-repulsion interaction. The $\Delta E_{\rm orb}$ represents the charge transformation and orbital mixing effects involved in fragments. The $\Delta E_{\rm c}$ is coulomb dependent term, including the contribution of coulomb correlation effects to the intersegment interaction energy and the dispersion correction energy.

In addition, based on the experimental crystal structure, 1a and two center moieties of 1a

 $(\{Nb_{13}O_{42}\}, \{(TeO_3)_{12}Nb_{13}O_{42}\})$ has been simplified as the calculation models. The corresponding electronic structure was calculated at $SMD^{[13]}(H_2O)/MN15/[6-31G(d)^{[18]}/SDD^{[19]}(Nb, Te)]$ level to obtain the molecular orbitals and molecular energy levels. Images of the molecular orbitals were prepared with Multiwfn^[20] and $VMD^{[21]}$ visualization programs.

Table S13. Results of EDA analyses of $\{Nb_2O_9\}$, $\{Nb_2O_{10}\}$, $\{Nb_2O_{11}\}$ and $\{(TeO_3)_2Nb_2O_9\}$ species.

$\Delta E \text{ (eV)}$	${\bf Nb_2O_9}$	${ m Nb_2O_{10}}$	${\bf Nb_2O_{11}}$	$\{(TeO_3)_2Nb_2O_9\}$
ΔE_{int}	-82.12	-87.30	-89.91	-82.49
$\Delta oldsymbol{E_{els}}$	-73.44	-77.75	-79.73	-67.47
$\Delta oldsymbol{E}_{orb}$	-12.55	-13.24	-13.74	-18.69
$\Delta oldsymbol{E}_c$	-0.50	-0.49	-0.48	-0.47
ΔE_{xrep}	4.39	4.18	4.04	4.15

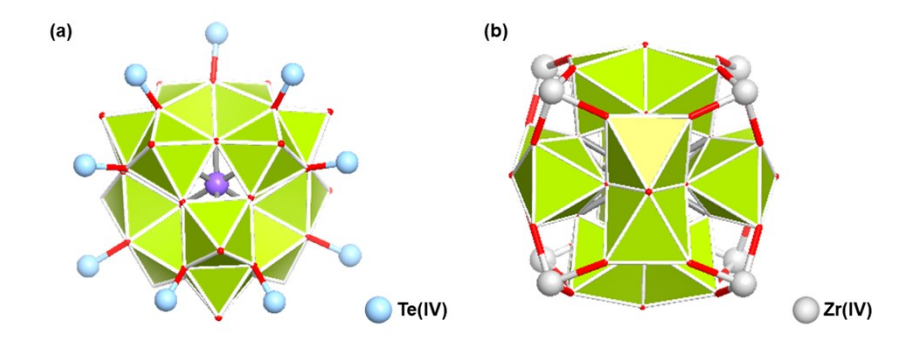


Figure S33. The structures of $\{Nb_{13}O_{42}\}$ stabilized by Te(IV) in compound 1 (a) and $\{BaNb_{12}O_{42}\}$ stabilized by Zr(IV) in natural mineral (b).

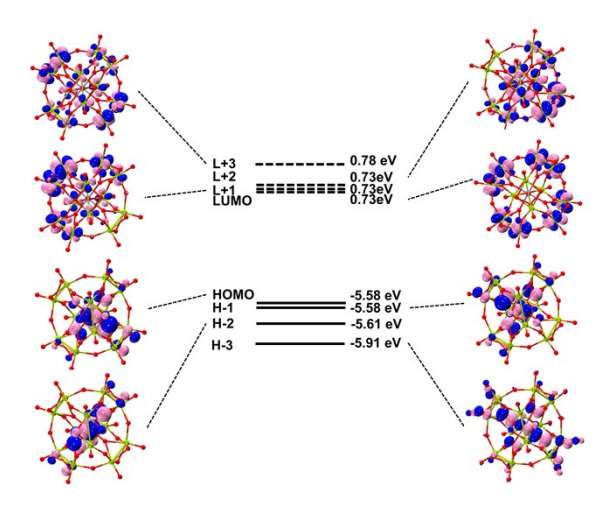


Figure S34. The frontier molecular orbitals and orbital energy levels of $\{Nb_{13}O_{42}\}$.

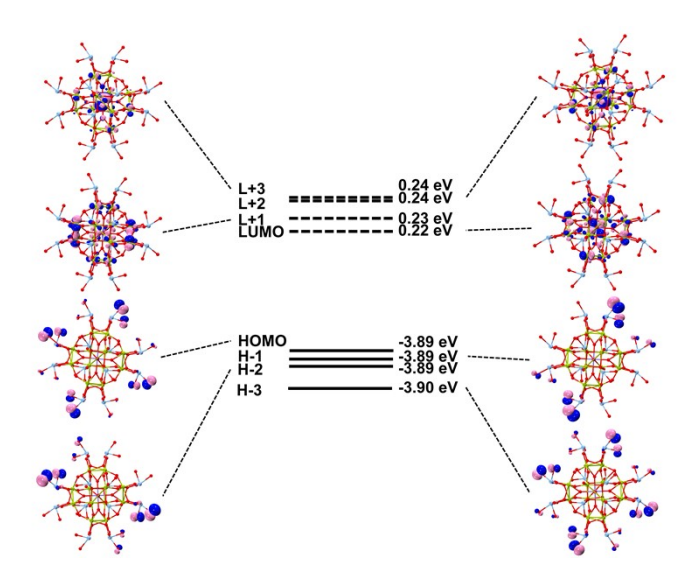


Figure S35. The frontier molecular orbitals and orbital energy levels of Te-coordinated $\{(TeO_3)_{12}Nb_{13}O_{42}\}.$

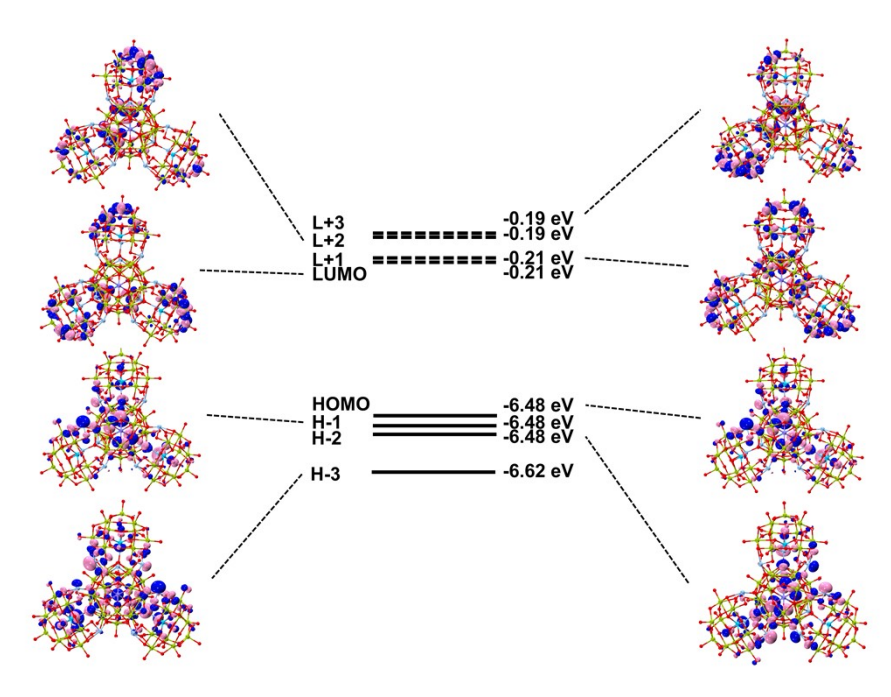


Figure S36. The frontier molecular orbitals and orbital energy levels of 1a.

IX. Photocatalytic hydrogen evolution performance

Table S14. Comparative experiments under different conditions for the photocatalytic H_2 evolution of 1.

Entry	Catalysts	Solvents	SD	PS	H₂ Rate (μmol g ⁻¹ h ⁻¹)
1	1	MeCN+H ₂ O	TEA	/	n.d.
2	1	MeCN+H ₂ O	/	$[Ru(bpy)_3]Cl_2 \cdot 6H_2O$	n.d.
3	1	MeCN	TEA	$[Ru(bpy)_3]Cl_2 \cdot 6H_2O$	n.d.
4	1	H_2O	TEA	$[Ru(bpy)_3]Cl_2 \cdot 6H_2O$	n.d.
5	1	MeCN+H ₂ O	TEA	$[Ru(bpy)_3]Cl_2 \cdot 6H_2O$	Trace
6	/	MeCN+H ₂ O	TEA	$[Ru(bpy)_3]Cl_2 \cdot 6H_2O$	Trace

Reaction conditions: 1 (10 mg), SD = triethylamine (TEA), PS = $[Ru(bpy)_3]Cl_2 \cdot 6H_2O$ (10 mg), MeCN + H_2O (28 mL + 2 mL), Ar (1 atm), λ = 300-1100 nm, 25 °C, 4 h, n.d. = Not detectable. 1. without photosensitizers; 2. without sacrificial agent; 3. without H_2O ; 4. without MeCN; 5. in the dark; 6. without any catalyst.

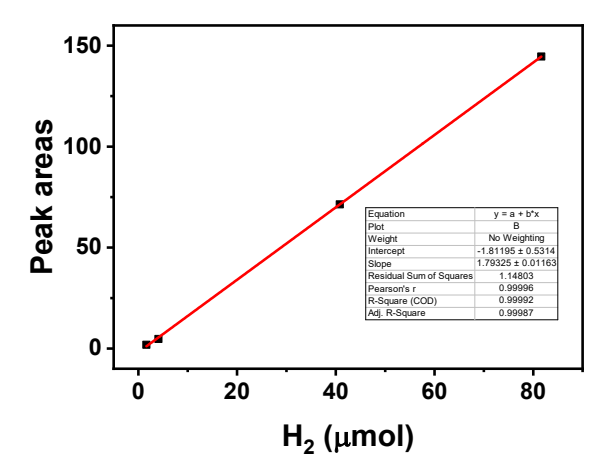


Figure S37. The standard curve of H_2 .

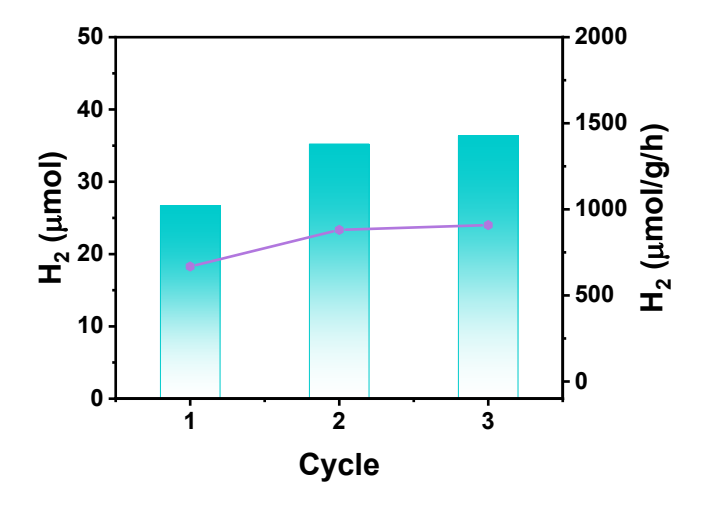


Figure S38. Recycling tests of H₂ production over 1.

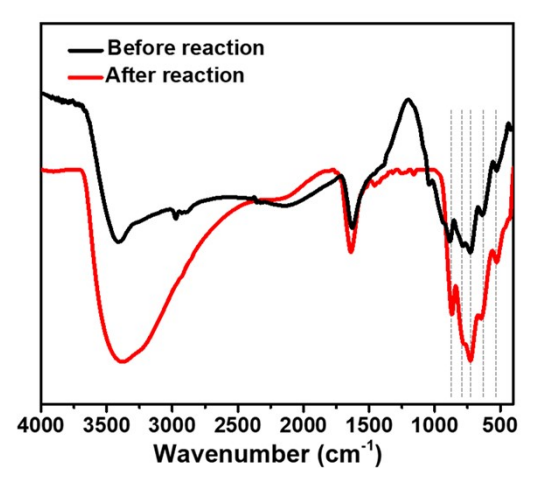


Figure S39. FT-IR spectra of 1 before (black) and after (red) the photocatalytic reaction test.

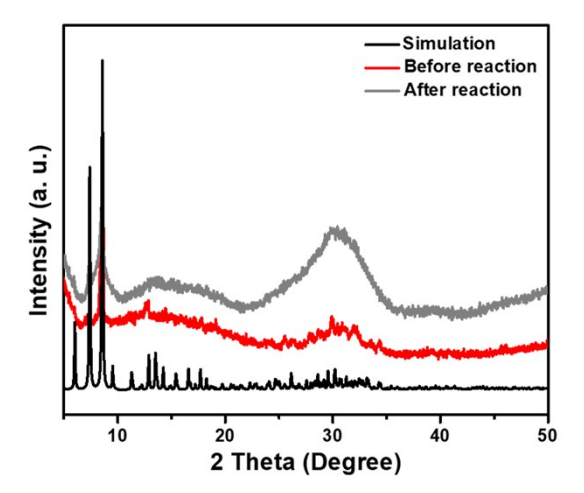


Figure S40. PXRD patterns of **1** before (red) and after (grey) the photocatalytic reaction test compared with the simulated one (black). The crystallinity of the recycled catalyst dramatically decreased compared with fresh samples, but some main peaks still match with the simulated ones.

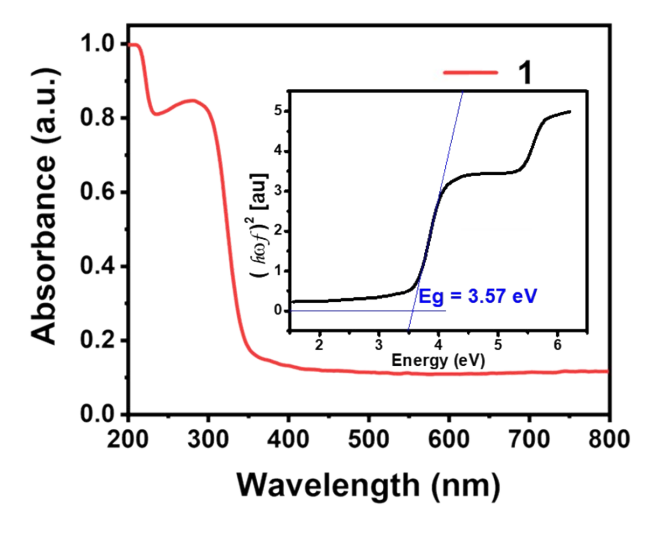


Figure S41. The UV-vis absorption spectrum of **1**. The inset displays the Kubelka-Munk curve.

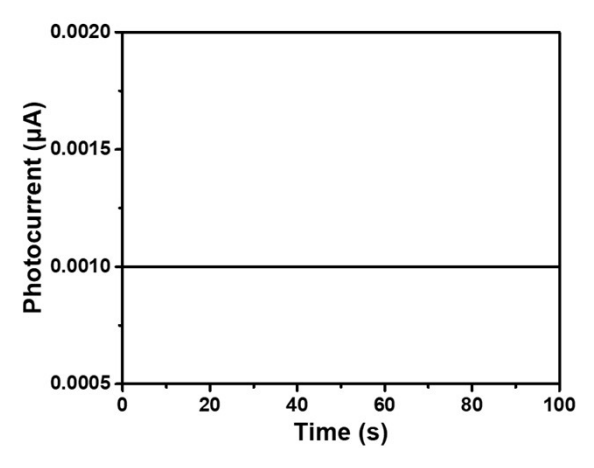


Figure S42. Transient photocurrent response of K₇HNb₆O₁₉.

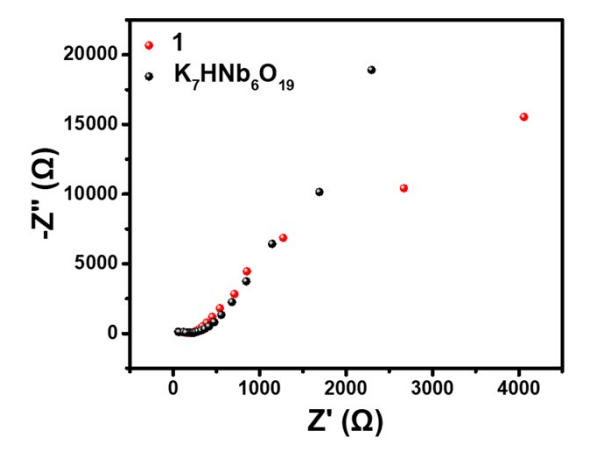


Figure S43. Electrochemical impedance spectroscopy (EIS) spectra of 1 and $K_7HNb_6O_{19}$.

References

- [1] C. M. Flynn, G. D. Stucky, Inorg. Chem. 1969, 8, 332-334.
- [2] N. Zhen, J. Dong, Z. G. Lin, Z. Li, C. P. Liu, X. X. Li, W. J. Geng, Y. N. Chi, and C. W. Hu, *Chem. Eur. J.* **2023**, e202203903.
- [3] a) G. M. Sheldrick, *SHELXL-97, a program for crystal structure refinement*. University of Göttingen, Göttingen, 1997; b) G. M. Sheldrick, *Acta Crystallogr., Sect. A* 2008, 64, 112; c) G. M. Sheldrick, *Acta Crystallogr. C: Struct. Chem.* 2015, 71, 3-8; d) O. V. Dolomanov, L. J. Bourhis, R. J. Gildea, J. A. K. Howard, H. Puschmann, *J. Appl. Cryst.* 2009, 42, 339-341.
- [4] A. L. Spek, Acta Cryst. 2015, C71, 9-18.
- [5] M. T.-K. Ng, N. L. Bell, D. L. Long, L. Cronin, J. Am. Chem. Soc. 2021, 143, 20059-20063.
- [6] M. Nyman, P. C. Burns, Chem. Soc. Rev. 2012, 41, 7354-7367.
- [7] I. D. Brown, D. Altermatt, Acta Cryst. 1985, B41, 244-247.
- [8] L. Jin, Z. K. Zhu, Y. L. Wu, Y. J. Qi, X. X. Li, S. T. Zheng, *Angew. Chem. Int. Ed.* **2017**, *56*, 16288-16292.
- [9] R. P. Bontchev, M. Nyman, Angew. Chem. Int. Ed. 2006, 45, 6670-6672.
- [10] Z. J. Liang, Y. Z. He, Y. Y. Qiao, P. T. Ma, J. Y. Niu, J. P. Wang, *Inorg. Chem.* **2020**, *59*, 7895-7899.
- [11] Y. L. Wu, Z. H. Zhong, P. X. Wu, Y. Q. Sun, X. X. Li and S. T. Zheng, *Eur. J. Inorg. Chem.* **2021**, 2021, 1505-1509.
- [12] P. V. Konarev, V. V. Volkov, A. V. Sokolova, M. H. J. Koch, D. I. Svergun, *J. Appl. Cryst.* **2003**, 36, 1277-1282.
- [13] H. S. Yu, X. He, S. L. Li, D. G. Truhlar, Chem. Sci. 2016, 7, 5032-5051.
- [14] A. V. Marenich, C. J. Cramer, D. G. Truhlar, J. Phys. Chem. B 2009, 113, 6378-6396.
- [15] F. Yu, L. X. Fu, Y. Yang, Int. J. Quantum Chem. 2017, 117.
- [16] T. Lu, Q. Chen, J. Phys. Chem. C 2023, 127, 7023-7035.
- [17] E. D. Glendening, C. R. Landis, F. Weinhold, Wires Comput. Mol. Sci. 2012, 2, 1-42.
- [18] P. C. Hariharan, J. A. Pople, *Theoret. Chim. Acta* 1973, 28, 213-222.
- [19] M. Mu, H. Gao, Spectrochem. Acta A 2021, 261.
- [20] T. Lu, F. Chen, J. Comput. Chem. 2012, 33, 580-592.
- [21] W. Humphrey, A. Dalke, K. Schulten, J. Mol. Graph Model 1996, 14, 33-38.